



Brightness Behavior of Distant Oort Cloud Comets

Carrie E. Holt^{1,2,14} , Matthew M. Knight^{2,3} , Michael S. P. Kelley² , Tim Lister¹ , Quanzhi Ye (叶泉志)^{2,4} ,
Colin Snodgrass⁵ , Cyrielle Opitom⁵ , Rosita Kokotanekova⁶ , Megan E. Schwamb⁷ , Matthew M. Dobson⁷ ,
Michele T. Bannister⁸ , Marco Micheli⁹ , Stefanie N. Milam¹⁰ , Derek C. Richardson²

(The LCO Outbursting Objects Key (LOOK) Project),

Edward Gomez¹¹ , Joseph P. Chatelain¹ , and Sarah Greenstreet^{12,13}

¹ Las Cumbres Observatory, 6740 Cortona Drive, Suite 102, Goleta, CA 93117, USA; cholt@lco.global

² Department of Astronomy, University of Maryland, College Park, MD 20742, USA

³ Physics Department, United States Naval Academy, 572C Holloway Road, Annapolis, MD 21402, USA

⁴ Center for Space Physics, Boston University, 725 Commonwealth Avenue, Boston, MA 02215, USA

⁵ Institute for Astronomy, University of Edinburgh, Royal Observatory, Edinburgh, EH9 3HJ, UK

⁶ Institute of Astronomy and National Astronomical Observatory, Bulgarian Academy of Sciences, 72 Tsarigradsko Shose Boulevard, 1784 Sofia, Bulgaria

⁷ Astrophysics Research Centre, School of Mathematics and Physics, Queen's University Belfast, Belfast BT7 1NN, UK

⁸ School of Physical and Chemical Sciences—Te Kura Matū, University of Canterbury, Private Bag 4800, Christchurch 8140, New Zealand

⁹ ESA NEO Coordination Centre, Largo Galileo Galilei, 1, 00044 Frascati (RM), Italy

¹⁰ Solar System Exploration Division, Astrochemistry Laboratory Code 691, NASA Goddard Space Flight Center, 8800 Greenbelt Road, Greenbelt, MD 20771, USA

¹¹ Las Cumbres Observatory, School of Physics and Astronomy, Cardiff University, Queens Buildings, The Parade, Cardiff CF24 3AA, UK

¹² Rubin Observatory/NSF's NOIRLab, 950 North Cherry Avenue, Tucson, AZ 85719, USA

¹³ Department of Astronomy and the DIRAC Institute, University of Washington, 3910 15th Avenue NE, Seattle, WA 98195, USA

Received 2024 May 8; revised 2024 October 14; accepted 2024 October 31; published 2024 December 10

Abstract

Dynamically new comets provide important insights into the conditions of the presolar nebula and its evolution, as they are believed to have experienced minimal solar heating before their discovery. Since 2020 August, the Las Cumbres Observatory (LCO) Outbursting Objects Key Project has utilized LCO's network of 1 m telescopes to consistently monitor long-period comets (LPCs) discovered inbound beyond 5 au from the Sun approximately every 3 days in order to characterize the brightness evolution, colors, and coma morphology of distant comets over a range of heliocentric distances. We report the long-term time-series photometry of 21 objects in our sample and coma morphology analyses for six comets with heliocentric distances less than 3 au. We find that LPCs rapidly brighten further from the Sun, and the brightening rate decreases as heliocentric distance decreases. We do not observe a clear difference in brightening rate for returning versus dynamically new comets. When LPCs are within 3 au of the Sun, they consistently exhibit a color change in a 20,000 km aperture consistent with an increase in gas production driven by water-ice sublimation. We find that returning comets experience the color change closer to the Sun than dynamically new comets, likely because their volatiles are more deeply buried or they have a higher dust-to-gas ratio after the upper layers are depleted of volatiles during a previous solar passage.

Unified Astronomy Thesaurus concepts: Comets (280); Long period comets (933); Comet volatiles (2162); Broad band photometry (184); Optical observation (1169)

1. Introduction

The majority of observed comets fall into one of two types: Jupiter-family comets (JFCs), which evolve from the trans-Neptunian region, and long-period comets (LPCs), which are perturbed inward from the Oort cloud by passing stars and galactic tides. When a comet enters the planetary region of the solar system ($r_h \lesssim 40$ au), solar irradiation will induce the outgassing of volatiles, which can cause cometary nuclei to undergo physical changes (e.g., J.-B. Vincent et al. 2016a), as well as chemical changes (e.g., L. Feaga et al. 2007; M. F. A'Hearn et al. 2011). JFCs have had numerous orbits within the inner solar system with dynamical lifetimes of around 10,000 yr (H. Rickman et al. 1992; J. A. Fernández et al. 2002; S. Lowry et al. 2008), resulting in observable

evolutionary properties that are consistent with prolonged exposure to temperatures well above the sublimation point of water (see review in A. Guilbert-Lepoutre et al. 2015; G. Filacchione et al. 2022). On the other hand, LPCs are relatively unprocessed compared to JFCs due to highly elongated orbits spanning hundreds to millions of years. Some LPCs have had previous passages through the inner solar system and are therefore processed to some extent. Other LPCs entering the inner solar system for the first time are considered to be “dynamically new” comets (DNCs). DNCs are valuable probes for connecting observed cometary properties to conditions in the presolar nebula and subsequent evolution, as they are considered to be mostly primitive with limited solar heating prior to discovery.

DNCs are a subset of LPCs distinguished by their orbital properties. Historically, the original orbital energy has been used as the main diagnostic. The original orbital energy of an LPC is proportional to the inverse of the original semimajor axis, $1/a_0$, with respect to the barycenter of the solar system, which is calculated by integrating the orbit backward in time until it reaches a distance from the Sun where planetary perturbations are negligible (~ 250 au). A negative $1/a_0$

¹⁴ LSST-DA Catalyst Postdoctoral Fellow.

indicates an interstellar (unbound) object; however, the vast majority of negative $1/a_0$ values are consistent with a bound orbit within the uncertainties. The distribution of $1/a_0$ shows an excess of comets with $a_0 > 10^4$ au. This “spike” led to the postulation of the Oort cloud (J. H. Oort 1950; J. H. Oort & M. Schmidt 1951).

However, recent studies have shown that not all comets in the Oort spike are truly pristine, and constructing accurate dynamical models is more challenging than previously suggested (P. A. Dybczyński & M. Królikowska 2015; P. A. Dybczyński & S. Breiter 2022). There is no discriminating value of $1/a_0$ separating new and returning comets, and $1/a_0$ does not directly correlate with previous perihelion distance q_{prev} (though comets with $1/a_0 < 3 \times 10^{-5} \text{ au}^{-1}$ are more likely to have $q_{\text{prev}} > 20$ au; P. A. Dybczyński & M. Królikowska 2015). Therefore, a ground-based observational diagnostic that can distinguish new from returning comets, separate from dynamical models, would be extremely valuable.

O. Harrington Pinto et al. (2022) compiled CO and CO₂ production rates for 25 comets and Centaurs, including 14 LPCs. They found that DNCs have a lower CO/CO₂ ratio compared to returning LPCs and proposed that CO/CO₂ may be used as a diagnostic for dynamical age. However, CO₂ can only be directly measured using space-based observatories, and while forbidden oxygen line [O I] ratios can be used to determine the CO₂ production rate, the comet must be bright enough with a large enough geocentric Doppler shift for such a detection. Additionally, the release rates of [O I] from H₂O, CO₂, and CO are not well known at this time (see Section 4.2 in A. J. McKay et al. 2016). Therefore, this method cannot viably be applied to large numbers of comets, whereas broadband optical photometry can be applied to fainter comets using smaller facilities.

Differences in the brightening rates between new and returning comets have been observed since the introduction of the Oort cloud hypothesis (J. H. Oort & M. Schmidt 1951). Several studies (F. L. Whipple 1978; M. F. A’Hearn et al. 1995) found that returning comets typically brighten more rapidly than DNCs, but these studies were limited to observations within 3 au, where activity is driven by water-ice sublimation. Recent sky surveys now routinely discover comets at greater heliocentric distances, where activity is likely driven by more volatile ices such as CO and CO₂ (K. J. Meech & J. Svoren 2004; M. Womack et al. 2017; D. Jewitt et al. 2021), although the exact mechanisms remain poorly understood. Limited studies at these distances (K. J. Meech et al. 2009; K. Sárneczky et al. 2016) suggest that DNCs tend to exhibit higher activity levels than returning comets, but comprehensive orbital coverage is lacking.

Starting in the region where water-ice sublimation cannot be the primary source of activity, we characterized the brightness behavior of LPCs across a range of heliocentric distances, comparing DNCs and returning LPCs. We achieved this by utilizing Las Cumbres Observatory’s (LCO) network of 1 m telescopes with data taken as part of the LCO Outbursting Objects Key (LOOK) Project, which we describe further in Section 2.1. By using LCO, we have access to several telescopes of the same size (1 m) in both the Northern and Southern Hemisphere, which are equipped with standardized instruments and filters. To capture the temporal variations sufficiently, we conducted frequent observations (every 3 days)

over extended time frames (approximately 1 yr or longer) and a wide range of heliocentric distances ($\Delta r_h > 1$ au). We present our analysis on the evolution of photometric magnitudes, $g - r$ color, and coma morphology. We discuss our sample, observations, and reductions in Section 2 and our analysis methods in Section 3. We present our results in Section 4. Finally, we discuss the implications of our findings in Section 5 and conclude with a summary in Section 6.

2. Observations and Reduction

2.1. The LOOK Project

LCO manages a global network of robotic telescopes, currently consisting of two 2 m telescopes, 13 1 m telescopes, and 10 40 cm telescopes housed at six observatory sites in both the Northern and Southern Hemisphere. The network functions as a single, interconnected observing facility that uses a software scheduler to continuously optimize the observing schedule of each individual telescope. LCO supports a number of large, cohesive, multiyear observing programs called Key Projects¹⁵ that are developed to maximize the scientific results from the unique capabilities of the network.

The LOOK Project started as a 3 yr Key Project focused on the behavior of active small bodies across the solar system, utilizing LCO’s extensive network of robotic telescopes. The project was awarded over 1900 hr of observation time spanning from 2020B to 2023A and was later awarded another 1000 hr through 2024B. First-year results were presented in T. Lister et al. (2022). The project encompasses two main observing objectives: follow-up of outbursts on all types of solar system objects and long-term monitoring of distant LPCs. Here we present a summary of the observations and findings related to the LPC aspect of the LOOK Project during its initial 3 yr phase (until 2023 July 31). However, all objects (unless disintegrated) continue to be observed by LOOK’s extended phase, which will last through 2025 January.

2.2. Sample and Caveats

Comets included in this study were selected based on specific criteria: they were recently discovered inbound with a heliocentric distance $r_h \gtrsim 5$ au and were expected to experience a change in heliocentric distance of at least 1 au ($\Delta r_h \gtrsim 1$ au) before perihelion (Table 1). Minor Planet Electronic Circulars,¹⁶ which announce new discoveries, were continuously monitored to identify suitable targets according to these criteria. In most cases, we managed to observe a recently discovered comet within a few days of its announcement. During its initial 3 yr phase, LOOK monitored 29 LPCs. Of these, seven objects had not yet reached the minimum heliocentric distance required for this study, but they are still being observed for future analysis. Additionally, comet C/2014 UN 271 (Bernardinelli-Bernstein) has been monitored by LOOK since its discovery announcement, where our team found it to be active at $r_h = 20$ au (R. Kokotanekova et al. 2021). However, because its perihelion distance is greater than 10 au (significantly beyond the heliocentric distance range of this study) and its distance has changed proportionally little, we do not include it in our comparison. A summary of the first 9 months of LOOK observations of C/2014 UN 271 was presented by

¹⁵ <https://lco.global/science/keyprojects>

¹⁶ <https://www.minorplanetcenter.net/mpec/RecentMPECs.html>

Table 1
LPCs Monitored by the LOOK Project

Name	T_0^a	r_0^b (au)	q^c (au)	r_h^d (au)	$\Delta_{r_h}^e$ (au)	$1/a_0^f \times 10^6$		
						N	M	C
C/2019 F1 (ATLAS–Africano)	2020 Aug 13	4.55	3.59	7.33	4.70	28	−68	39
C/2019 L3 (ATLAS)	2020 Aug 31	5.59	3.55	5.81	4.30	27	108	27
C/2020 O2 (Amaral)	2020 Aug 3	5.71	4.86	7.11	3.23	31	−108	44
C/2020 R7 (ATLAS)	2020 Sep 30	7.03	2.95	4.25	5.38	13	−127	21
C/2020 U4 (PANSTARRS)	2020 Nov 1	5.65	5.35	6.39	1.34	12	22	22
C/2021 A1 (Leonard)	2021 Apr 8	3.55	[0.61] ^g	0.85	2.70	490	383	...
C/2021 C5 (PANSTARRS)	2021 Mar 28	6.78	3.24	3.60	3.90	18	−75	...
C/2021 E3 (ZTF)	2021 May 8	4.82	1.77	4.31	5.59	−2	−6	...
C/2021 G2 (ATLAS)	2021 Aug 13	9.44	[4.97]	5.99	3.45	15	4	...
C/2021 O3 (PANSTARRS)	2021 Aug 3	4.20	[0.29] ^g	3.01	1.19	−42	−22	...
C/2021 S3 (PANSTARRS)	2021 Nov 5	8.60	[1.33]	3.97	4.63	15	1919	...
C/2021 T4 (Lemmon)	2021 Nov 8	6.90	1.48	1.48	5.42	33	4	...
C/2021 Y1 (ATLAS)	2022 Jan 7	5.42	[2.03]	2.04	3.38	8	−11	...
C/2022 A2 (PANSTARRS)	2022 Mar 2	4.41	1.73	2.67	3.62	3	15	...
C/2022 A3 (ATLAS)	2022 May 15	5.66	[3.70]	3.82	1.84	1153	1164	...
C/2022 E2 (ATLAS)	2022 Apr 2	8.14	[3.66]	5.38	2.67	71	−1	...
C/2022 E3 (ZTF)	2022 Mar 22	4.07	1.11	1.91	3.76	713	768	...
C/2022 L2 (ATLAS)	2022 Jun 22	6.47	[2.76]	3.54	2.93	10	23	...
C/2022 R6 (PANSTARRS)	2022 Nov 5	9.34	[6.57]	8.25	1.09	29	106	...
C/2022 T1 (Lemmon)	2023 Feb 10	4.80	[3.44]	4.07	0.73	6	84	...
C/2023 A3 (Tsuchinshan–ATLAS)	2023 Mar 1	7.25	[0.39]	5.85	1.40	14	−214	...

Notes.

^a UT date of first LOOK observation.

^b Heliocentric distance of first LOOK observation.

^c Perihelion distance; brackets indicate that the comet has not yet reached perihelion.

^d Heliocentric distance of latest LOOK observation (as of 2023 July 31).

^e Total range of heliocentric distance observed by LOOK: $r_0 - r_h$ if the comet has not yet reached perihelion or $(r_h - q) + (r_0 - q)$ if it has.

^f The reciprocal original semimajor axis in au^{-1} according to Nakano Note (N), Minor Planet Center (M), and CODE Catalog (C).

^g C/2021 A1 and C/2021 O3 disintegrated preperihelion.

M. S. P. Kelley et al. (2022). Thus, the sample studied here includes 21 comets (Figure 1).

To ensure accurate comparisons across varying heliocentric distances and between different comets, as well as to streamline the analysis of our extensive data set containing over 7000 images from 21 comets, we relied on batch photometric processing as our primary method. However, this approach limited our ability to optimize techniques for each individual image, especially given the diverse range of comets and heliocentric distances in our sample. For instance, while an aperture size of 20,000 km might appear appropriate for comets located between 2 and 3 au from Earth, where the angular size ranges from approximately $9''$ to $14''$, our observations encompass a wide range from beyond 8 au to within 1 au of Earth, resulting in angular sizes ranging from less than $3''$ to more than $28''$ for a 20,000 km aperture. The situation is reversed when using a constant angular aperture size of $5''$, as it fails to capture the entirety of the coma during observations near Earth. Ultimately, we selected the most suitable parameters for the majority of the data set ($5''$ aperture for long-term photometry and 20,000 km aperture for color analysis), while also taking into account the potential impact of those choices on our findings.

2.3. Instruments

Observations were taken with LCO’s global network of 1 m robotic telescopes located at six different observatory sites spanning both the Northern and Southern Hemisphere

(T. M. Brown et al. 2013). An identical Sinistro imager is mounted on each telescope, which includes a 4096×4096 pixel CCD with a $26' \times 26'$ field of view, resulting in a pixel scale of $0''.39 \text{ pixel}^{-1}$. Sloan Digital Sky Survey (SDSS) g' and r' filters were used to probe the gas and dust components of the coma: the SDSS g' filter covers C_2 and C_3 emission bands, whereas the r' filter is mostly free of strong gas emission lines (see Figure 3 in T. Lister et al. 2022).

2.4. Data Collection

Once selected, the targets were scheduled for observations to occur every 3 days with ± 18 hr flexibility using the NEOExchange observation manager (T. A. Lister et al. 2021). Because LCO covers both hemispheres, the only major gaps in otherwise continuous coverage were when the comet reached a solar elongation of less than 60° , which typically lasted ~ 4 months, depending on the individual orbit geometry. Other constraints included an apparent V magnitude brighter than ~ 20 mag and a target–observer–Moon angle greater than 45° . We did not have additional constraints on observing conditions outside of LCO’s standard thresholds. Each visit consisted of two exposures per filter made at the rate of motion of each object, typically $\lesssim 1'' \text{ minute}^{-1}$. Exposure times were nominally ~ 180 s but were shortened if tracking the proper motion of the comet would produce star streaks longer than $2''$ to ensure accurate astrometry, as our average seeing was $2''\text{--}3''$.

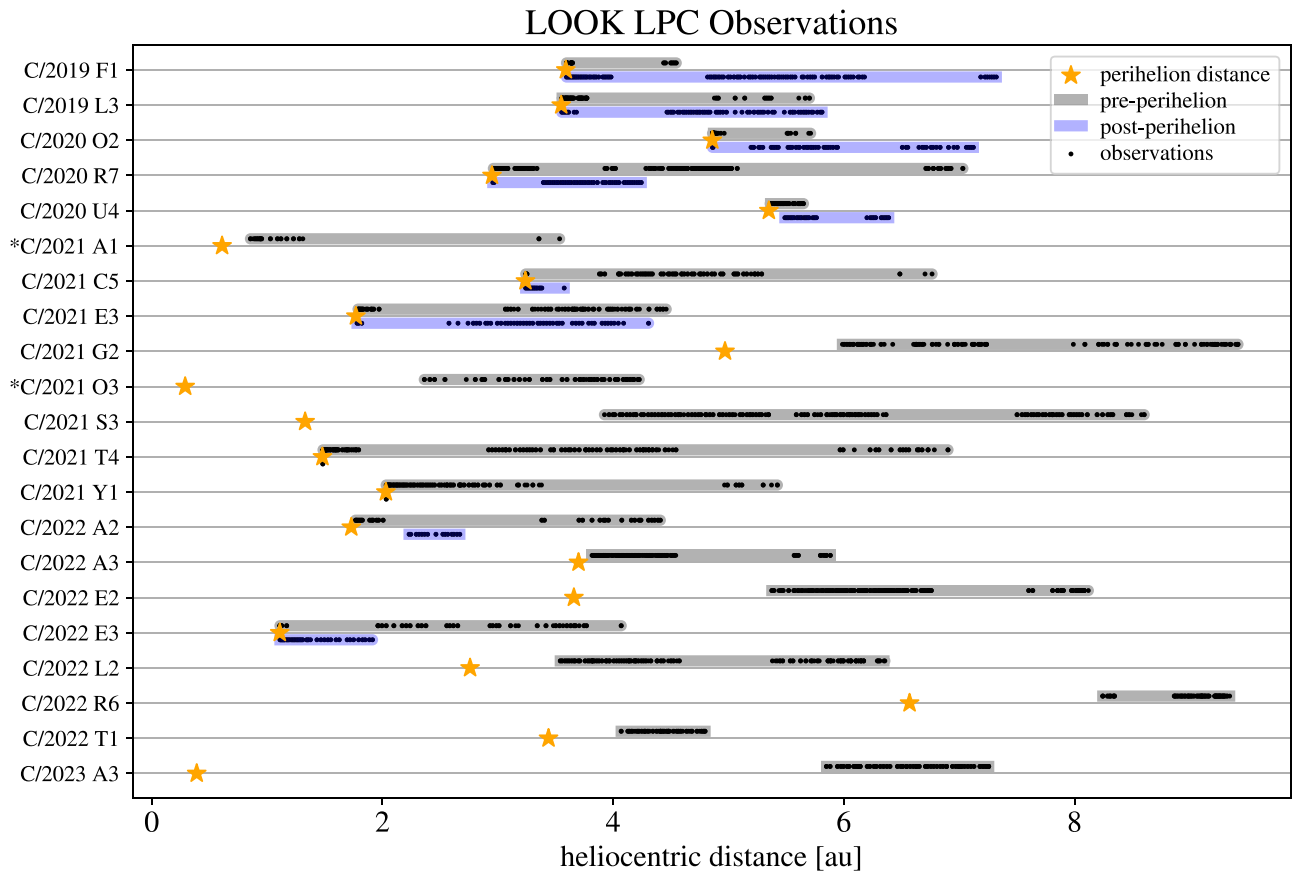


Figure 1. A visualization of the heliocentric range of observations for each comet discussed in this paper. Each black point represents one visit. The shaded regions show the preperihelion range (gray) and postperihelion range (blue), where the yellow stars are the perihelion distance for each comet. The asterisks represent comets that disintegrated. Observations are continuing for all nondisintegrated comets.

2.5. Data Reduction

Newly acquired images were automatically pipeline-processed by LCO’s Beautiful Algorithms to Normalize Zillions of Astronomical Images (BANZAI) pipeline (C. McCully et al. 2018), which performs basic CCD reduction (bias and dark subtraction and flat-field correction) as well as source extraction and astrometric calibration. The data were then fed into a pipeline based at the University of Maryland (T. Lister et al. 2022) to conduct the photometric analysis described below.

The BANZAI catalog was used to photometrically correct each image, calibrating the image to the Pan-STARRS1 (PS1) photometric system (J. L. Tonry et al. 2012) using the CALVIACAT software (M. S. P. Kelley & T. Lister 2022), the ATLAS-RefCat2 photometric catalog (J. L. Tonry et al. 2018), and LOOK Project–derived color corrections. The photometry pipeline considered a color correction owing to the difference between the PS1 filters used by ATLAS-RefCat2 and the SDSS filter set used at the LCO telescopes. The color corrections used to convert instrumental magnitudes to PS1 magnitudes were -0.086 ± 0.035 for g and 0.021 ± 0.018 for r . The color corrections were determined from the analysis of over 1000 images in each color band, and the errors are the standard deviation (see Section 5 in T. Lister et al. 2022). Photometry calibrated to the PS1 system using AB magnitudes is hereafter denoted g and r .

The pipeline automatically ignored images that encountered processing issues, such as a missed target, an invalid World

Coordinate System solution, or cases with too few stars for calibration. The remaining images were manually inspected for contamination by passing stars or scattered lunar light. If the image could be calibrated, photometry was attempted on the comet centroid. If centroiding failed, the ephemeris position was used. In all cases, the final aperture center was visually inspected and found to be accurate.

For our time-series photometry, we used the weighted average (which accounts for varying uncertainties by giving more weight to measurements with smaller errors, specifically using weights of $1/\sigma^2$) of the photometry for the visit and chose an aperture radius of $5''$, which is $\sim 15,000$ km at a geocentric distance of 4 au, because a fixed physical size aperture would be too small at large r_h . However, an aperture with a fixed angular size is not ideal for color evolution studies, as dust brightness nominally falls as $1/\rho$, while gas is usually flatter. Therefore, a larger aperture will generally contain a larger proportion of gas to dust compared to a smaller aperture that only captures the inner coma. For our assessment of color evolution (see Section 4.2), we mitigated this by using a photometric aperture of 20,000 km so that we probed color changes occurring within the same coma radius, regardless of r_h . In most of our observations, the coma typically filled both apertures. At heliocentric distances beyond 8 au, the $5''$ aperture contained more background signal, while the coma continued to fill or extend beyond the smaller 20,000 km aperture. Closer to the Sun, the coma often extended beyond the $5''$ aperture but was generally contained within the 20,000 km aperture. Overall, we found the $5''$ aperture to yield the most consistent

results for photometric analysis across our data set, while the 20,000 km aperture was most suitable for color analysis.

We limited our analysis to images with a point-source full width at half-maximum (FWHM) of $\leq 4.''0$ and final photometric errors of ≤ 0.15 mag, which collectively ignored $\sim 7\%$ of the observations. While fainter targets were detectable in the images, the signal-to-noise ratio was too low for inclusion in the photometric studies presented here. We found our limiting magnitude to be ~ 21.4 and ~ 21.0 in the g and r filters, respectively.

3. Data Analysis

3.1. Activity

A commonly used reference normalization to ensure the most accurate comparisons for photometric magnitudes is $H(1, 1, 0)$, representing the theoretical brightness for a Sun-based observer with the comet at $r_h = 1$ au so that the comet–observer distance must be 1 au and the phase angle is equal to 0° . For our study, apparent magnitudes m_{app} were converted to heliocentric magnitudes m_{helio} , or $H(r_h, 1, 0)$, which is $H(1, 1, 0)$ without removing heliocentric dependencies. Because we used a fixed angular aperture size of $5''$, an aperture scaling is applied to account for the decreasing fractional flux in the aperture by altering the geocentric distance dependence, resulting in the final formula,

$$m'_{\text{helio}} = m_{\text{app}} - 2.5 \log_{10}(\Delta) + 2.5 \log_{10}(\phi(\alpha)), \quad (1)$$

where Δ equals the geocentric distance in au, α is the phase angle (the Sun–target–observer angle), and $\phi(\alpha)$ is the phase function, which is the ratio of the brightness at phase angle α to that at phase angle 0° . To calculate $\phi(\alpha)$, we used the Schleicher–Marcus phase function for cometary dust,¹⁷ which is a composite of the phase function from comet Halley (D. G. Schleicher et al. 1998) for smaller phase angles and the phase function derived for near-Sun comets in J. N. Marcus (2007a, 2007b) at mid-to-large phase angles (D. G. Schleicher & A. N. Bair 2011).

Each lightcurve was fit with a curve that follows

$$m'_{\text{helio}} = H(1, 1, 0) + 2.5n \log_{10}(r_h), \quad (2)$$

where $H(1, 1, 0)$ is the absolute magnitude and n is the activity index, which is used to quantify the brightness increase associated with heliocentric distance including geometric effects and activity (E. Everhart 1967). An object experiencing no change in the rate of activity would have an activity index of $n = 2$; i.e., brightness only increases due to the increasing amount of incident sunlight. We first modeled the entire data set for each comet for pre- and postperihelion using a least-squares fit to the r photometry and the g photometry shifted by the median color of the lightcurve. If the residuals of the fit were not contained within 2σ of the median magnitude error, then the lightcurve was fit with multiple n values. An n value of less than 2 indicates a decrease in intrinsic brightness, occasionally observed as a pre- or postperihelion peak in brightness. We found that using r data alone gave similar results to the combined r and g (shifted by the median color) data, including comparable residuals, as the scatter in both the g

and r data is approximately the same. Using the combined photometry allows us to make a more accurate fit when the data are more sparse. We were able to fit activity indices to the combined photometry for g and r because the color was constant beyond 3 au from the Sun for all comets. The only comets for which we determined activity indices within the heliocentric distance of the color change are C/2021 E3, C/2021 T4, and C/2022 A3. For these objects, the near-Sun heliocentric distances where the index was fit are relatively narrow, and the color variation is minimal, resulting in consistent indices within the uncertainties for the g and r filters, as well as their combined photometry.

We present the g and r photometry for each comet as an m'_{helio} lightcurve fitted with activity indices (n). An activity index was only determined when the data covered a large enough heliocentric distance range to do so ($\Delta r_h \gtrsim 1$ au). Additionally, there were gaps between observations where the activity index must be different from the n values reported before or after the gap, but since we did not have data at those times, we did not report an n value over those periods. However, we note that in some instances, a steeper brightness increase must have occurred during a gap in observations (C/2021 T4, C/2022 L2). The activity indices and corresponding heliocentric distance ranges for each comet are reported in Table 2. The g photometry in the lightcurve was shifted by the median $g - r$ color measured using a $5''$ aperture.

We also assessed the dust production using calculations of $Af\rho$, an aperture-independent quantity used as an estimator for dust production, which is the product of the albedo A , the filling factor f (i.e., how much the total cross section of grains fills the field of view), and the radius of the photometric aperture ρ (M. F. A'Hearn et al. 1984). We calculated $Af\rho$ from the brightness measurements using a solar magnitude of -26.93 in the PS1 r band. We then used the Schleicher–Marcus dust phase function (D. G. Schleicher & A. N. Bair 2011) to correct $Af\rho$ to a phase angle of 0° , $A(0^\circ)f\rho$. For most comets in our sample, the dust coma surface brightness profiles generally follow an approximate $1/\rho$ trend. However, for many of our distant observations, the coma did not extend far enough beyond the seeing disk to reliably measure any deviations from this trend.

3.2. Colors

By comparing the weighted average apparent magnitude in the g and r bandpasses, we were able to determine the $g - r$ color for each visit. We then assessed the variance of the $g - r$ color with respect to the median color across the range of heliocentric distances for each comet. All color measurements are reported in Table 3.

3.3. Coma Morphology

For the morphology analysis, we utilized nightly averaged (or median-combined if more than two) images. We generated images of coma gas by taking advantage of the presence of bright C_2 emission bands in the g filter and the absence of such bands in the r filter. We scaled an r image and subtracted it from the corresponding g image. The technique was previously demonstrated by T. Lister et al. (2022) with LOOK observations of comet C/2021 A1 (Leonard). The scale factor for each image was determined by trial and error and visual inspection.

¹⁷ <http://asteroid.lowell.edu/comet/dustphase.html>

Table 2
Activity Indices

Name	$1/a_0 \times 10^{6a}$	r_{\min}^b	r_{\max}^c	n^d
C/2019 F1 (ATLAS–Africano)	28	3.60	3.77	4.5 ± 0.2
		4.87	5.75	3.3 ± 0.1
		5.85	6.14	6.0 ± 0.2
C/2019 L3 (ATLAS)	27	-5.70	-4.88	6.5 ± 0.2
		-3.77	-3.56	7.8 ± 0.1
		4.48	4.89	5.4 ± 0.2
		4.91	5.63	4.5 ± 0.1
C/2020 O2 (Amaral)	31	5.27	5.94	3.6 ± 0.1
C/2020 R7 (ATLAS)	13	-5.08	-3.93	1.7 ± 0.1
		3.59	4.30	4.8 ± 0.1
C/2020 U4 (PANSTARRS)	12	-5.65	-5.36	...
		5.40	6.39	...
C/2021 A1 (Leonard)	490	-1.31	-0.86	...
C/2021 C5 (PANSTARRS)	18	-5.23	-4.05	5.1 ± 0.1
		3.24	3.55	3.5 ± 0.3
C/2021 E3 (ZTF)	-2	-4.46	-3.88	5.2 ± 0.1
		-3.65	-3.09	3.5 ± 0.1
		-1.97	-1.79	1.1 ± 0.1
		3.00	3.56	3.4 ± 0.1
C/2021 G2 (ATLAS)	15	-9.42	-8.09	7.0 ± 0.2
		-7.24	-6.12	3.6 ± 0.1
C/2021 O3 (PANSTARRS)	-42	-4.18	-3.56	5.6 ± 0.2
		-3.56	-3.01	2.5 ± 0.5
C/2021 S3 (PANSTARRS)	15	-8.58	-7.50	6.2 ± 0.2
		-6.26	-5.01	3.6 ± 0.1
		-4.98	-3.96	2.3 ± 0.1
C/2021 T4 (Lemmon)	33	-4.38	-2.92	1.9 ± 0.1
		-1.77	-1.50	0.0 ± 0.1
C/2021 Y1 (ATLAS)	8	-3.02	-2.48	2.2 ± 0.1
C/2022 A2 (PANSTARRS)	3	-4.36	-3.38	3.7 ± 0.1
		-2.01	-1.91	7.9 ± 0.2
		-1.83	-1.77	2.8 ± 0.5
		2.25	2.67	4.3 ± 0.1
C/2022 A3 (ATLAS)	1153	-5.88	-4.02	4.4 ± 0.1
C/2022 E2 (ATLAS)	71	-8.08	-7.60	7.6 ± 0.3
		-6.70	-6.36	7.4 ± 0.2
		-6.39	-5.39	2.7 ± 0.1
C/2022 E3 (ZTF)	713	-3.48	-1.96	2.9 ± 0.1
		1.17	1.64	3.6 ± 0.1
C/2022 L2 (ATLAS)	10	-6.04	-5.43	2.8 ± 0.2
		-4.42	-3.54	1.3 ± 0.1
C/2022 R6 (PANSTARRS)	29	-9.30	-8.87	9.8 ± 0.4
C/2022 T1 (Lemmon)	6	-4.68	-4.13	3.5 ± 0.1
C/2023 A3 (Tsuchinshan–ATLAS)	14	-7.25	-6.73	10.4 ± 0.1
		-6.37	-5.78	4.6 ± 0.1

Notes.^a Reciprocal original semimajor axis $\times 10^6 \text{ au}^{-1}$ according to Nakano Note.^b Starting heliocentric distance where a negative value represents preperihelion.^c Ending heliocentric distance where a negative value represents preperihelion.^d Activity index as defined in Equation (2) determined by least-squares fit with 1σ errors.

A successful optimization produced a gas image without signs of a dust tail. The scale factor yielded a “dust” color that differed from the standard aperture color, consistent with the presence of gas emission in the g bandpass. The scale factor varied for each comet, as detailed in Section 4.3. Images were further enhanced by subtracting the azimuthal median

(D. G. Schleicher & T. L. Farnham 2004; N. H. Samarasinha & S. M. Larson 2014) to eliminate bulk brightness and highlight subtle brightness variations. Some examples of asymmetries in the coma include jets, fans, and spirals (see D. G. Schleicher & T. L. Farnham 2004).

3.4. Dynamical Age

The CODE Catalog¹⁸ (M. Królikowska & P. A. Dybczyński 2020) is the first catalog to contain cometary orbits covering three successive perihelion passes—previous, observed, and next—typically over 1–10 million yr, calculating all orbit parameters and including the implementation of nongravitational accelerations. Most of our objects did not have a large enough data arc to be included in the CODE Catalog, so we needed to use a different source. For the comets in our sample, we compared the $1/a_0$ values from two different sources: orbital computations by Syuichi Nakano published on the Nakano Note website¹⁹ and the Minor Planet Center (MPC) Database.²⁰ We compared the two sources with the $1/a_0$ values from nearly 300 Oort spike comets in the CODE Catalog (M. Królikowska & P. A. Dybczyński 2020). When we compared the $1/a_0$ distribution for our sample from both sources, we found that the Nakano Note values followed a distribution similar to the CODE distribution, with nearly all of the objects having $1/a_0 > 0$, while MPC values had a much wider range, with many objects having $1/a_0 < 0$ (Figure 2). This disparity could stem from different methods of dynamical modeling, as Nakano Note includes nongravitational effects and MPC may not. Neglecting the nongravitational effects tends to produce original orbits that appear more hyperbolic than they actually are (B. G. Marsden & Z. Sekanina 1973; M. Królikowska 2001). There are also likely discrepancies due to a difference between barycentric and heliocentric reference frames. The CODE Catalog uses a barycentric reference frame, while the MPC uses a heliocentric reference frame, and the Nakano Note reference frame is not stated. Because the distribution of Nakano Note $1/a_0$ values is a better match to the distribution of the values in the extensive and precise CODE Catalog, we use the Nakano Note $1/a_0$ values for this study. Furthermore, five objects in our sample are in the CODE catalog, and their $1/a_0$ values are more consistent with the Nakano Note values.

We note here the potential for bias in prior studies based on what different authors consider dynamically new versus returning. There may be a discrepancy in the $1/a_0$ value used as a threshold (e.g., 5×10^{-5} or 10^{-4} au^{-1}). Additionally, different sources can produce very different $1/a_0$ values as shown here. We discuss the uncertainties with $1/a_0$ further in Section 5.3. For our study, we use $1/a_0 = 4 \times 10^{-5} \text{ au}^{-1}$ as the threshold between new and returning.

4. Results

4.1. Activity

The activity index is observed to decrease with decreasing heliocentric distance. A Spearman rank correlation analysis, using the average of the minimum and maximum heliocentric distances associated with each preperihelion activity index,

¹⁸ <https://pad2.astro.amu.edu.pl/comets/>¹⁹ <https://www.oaa.gr.jp/~oaacs/nk.htm>²⁰ https://www.minorplanetcenter.net/db_search/

Table 3
Color and $Af\rho$

Name	$g - r^a$ (mag)		$A(0^\circ)f\rho$ (cm) ^b		
	5''	20,000 km	p10	Median	p90
C/2019 F1 (ATLAS–Africano)	0.50 ± 0.03	0.51 ± 0.04	688	1573	1757
C/2019 L3 (ATLAS)	0.48 ± 0.02	0.48 ± 0.02	10,445	20,241	30,516
C/2020 O2 (Amaral)	0.48 ± 0.04	0.49 ± 0.03	1049	1865	1976
C/2020 R7 (ATLAS)	0.51 ± 0.03	0.52 ± 0.03	505	1232	1356
C/2020 U4 (PANSTARRS)	0.55 ± 0.10	0.55 ± 0.10	250	314	377
C/2021 A1 (Leonard) ^c	0.47 ± 0.06	0.13 ± 0.21	636	1469	1718
C/2021 C5 (PANSTARRS)	0.49 ± 0.04	0.50 ± 0.06	60	187	276
C/2021 E3 (ZTF) ^c	0.48 ± 0.05	0.48 ± 0.17	435	848	1613
C/2021 G2 (ATLAS)	0.49 ± 0.07	0.49 ± 0.06	1670	3873	4882
C/2021 O3 (PANSTARRS)	0.48 ± 0.03	0.44 ± 0.07	74	105	135
C/2021 S3 (PANSTARRS)	0.56 ± 0.04	0.56 ± 0.03	996	2978	3256
C/2021 T4 (Lemmon) ^c	0.49 ± 0.08	0.48 ± 0.22	227	672	798
C/2021 Y1 (ATLAS) ^c	0.47 ± 0.02	0.40 ± 0.06	471	567	627
C/2022 A2 (PANSTARRS) ^c	0.42 ± 0.04	0.28 ± 0.10	216	2791	4597
C/2022 A3 (ATLAS)	0.51 ± 0.03	0.52 ± 0.04	386	574	646
C/2022 E2 (ATLAS)	0.48 ± 0.04	0.48 ± 0.03	1444	3784	4044
C/2022 E3 (ZTF) ^c	0.54 ± 0.03	0.52 ± 0.03	2479	3961	4695
C/2022 L2 (ATLAS)	0.51 ± 0.03	0.52 ± 0.03	658	965	1051
C/2022 R6 (PANSTARRS)	0.52 ± 0.08	0.51 ± 0.08	733	977	1599
C/2022 T1 (Lemmon)	0.52 ± 0.04	0.53 ± 0.06	208	242	254
C/2023 A3 (Tsuchinshan–ATLAS)	0.49 ± 0.02	0.49 ± 0.02	1480	2736	3572

Notes.^a Median $g - r$ color $\pm 1\sigma$ using a 5'' and 20,000 km aperture with the uncertainty as the standard deviation of the color across all observations.^b 10th, 50th, and 90th percentile of $A(0^\circ)f\rho$ values from the entire data set for each comet.^c Experienced a significant change (greater than 0.15 mag) in color during observations.

shows a significant positive correlation between heliocentric distance and activity index ($\rho = 0.57$, $p = 0.001$). This trend is evident for individual objects (Figures 3, 4, and 5) as well as for the entire sample (Figure 6). Two objects that do not fall into this trend are C/2019 L3 and C/2022 A2, which experienced a “surge” in brightness near perihelion. The activity index was seen to vary for all but two comets (C/2021 C5 and C/2022 T1), and those LPCs had the shortest heliocentric distance range of ~ 1 au. While most indices were between $n = 1$ and $n = 8$, which is consistent with previous studies (K. J. Meech & J. Svoren 2004), C/2022 R6 and C/2023 A3 had brightening rates of $n \sim 10$ during their earliest observations farther from the Sun. We find that preperihelion epochs have a wider range in activity indices compared to postperihelion (Figure 7). Even though we cannot compare the most distant observations because higher r_h are not yet observed postperihelion in our sample, we still find that within 7 au of the Sun, all postperihelion activity indices are greater than 3.2, while $\sim 40\%$ of the preperihelion n values within 7 au are below 3.2.

To compare with prior studies, we fit a singular activity index over all preperihelion observations for each object. We find that “new” and returning comets have similar n distributions, with an average activity index of $n = 4.2 \pm 1.9$ for DNCs and $n = 3.7 \pm 0.7$ for returning comets, where the uncertainties are the standard deviations (Figure 8). Furthermore, a Kolmogorov–Smirnov test, which compares the cumulative distributions of two samples to assess whether they are drawn from the same distribution, between the new and returning n values yields a p -value of 0.68, suggesting that the two samples could be drawn from the same distribution.

Previous studies have found values of $n = 2$ for “new” comets and $n = 4$ for returning comets (see, e.g., review by K. J. Meech & J. Svoren 2004). We discuss potential causes for the discrepancy in Section 5.3.

The $A(0^\circ)f\rho$ values for the entire sample range over 2 orders of magnitude throughout the observations (Table 3). While a broad range, it is consistent with prior studies such as M. F. A’Hearn et al. (1995) and U. Fink (2009), which both had $A(0^\circ)f\rho$ values of tens to thousands of cm for their samples. We see no trend with heliocentric distance except that more distant discoveries have higher $A(0^\circ)f\rho$ values to start, which is expected as more active targets are intrinsically brighter and can be discovered at greater distances than less active comets. We also find no clear trend with $1/a_0$ after visual inspection (Figure 9).

4.2. Colors

The average color of the sample when $r_h > 3$ au is $g - r = 0.51 \pm 0.03$ mag, which is consistent with other active LPCs (D. Jewitt 2015). We find no significant difference between new and returning comets (Figure 10). We also observe no trends with heliocentric distance until the comets reach $r_h \lesssim 3$ au.

A color change was measured in all objects that were observed within 3 au of the Sun (Figure 11). For these six objects, the color shifted bluer during their perihelion passages. We assessed the heliocentric distance where the color change occurred for all objects and found that the two returning comets, C/2021 A1 and C/2022 E3, changed color closer to the Sun ($r_h \lesssim 2$ au) compared to “new” comets. The four “new” comets that changed color did so around $r_h \sim 3$ au and followed

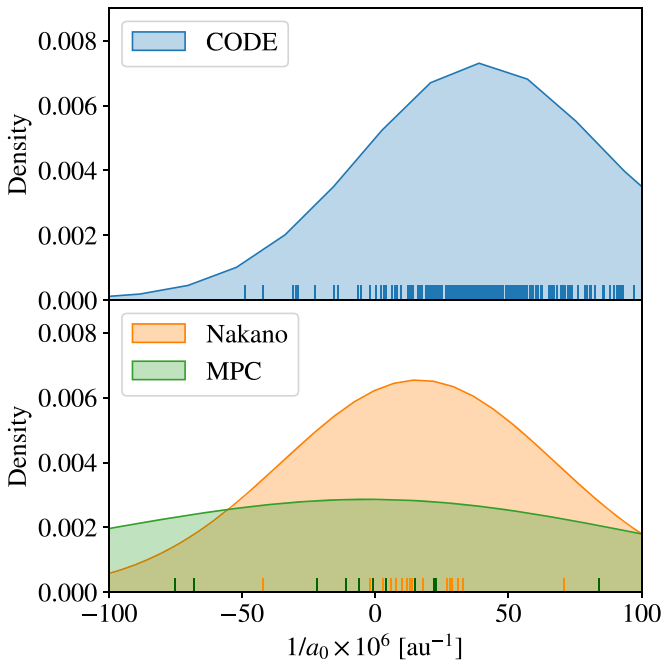


Figure 2. The bottom figure shows the distribution of $1/a_0$ values of our sample from two different sources, Nakano Note (orange) and MPC (green), which we compared to results for all comets from the CODE Catalog (P. A. Dybczyński & M. Królikowska 2016; top). The distributions are presented as a kernel density estimate plot. Rather than using discrete bins, a kernel density estimate plot smooths the measurements with a Gaussian kernel, producing a continuous probability density estimate. The lines at the bottom of the figure represent the individual values that make up the kernel density estimate and are present for all future kernel density estimate figures. The data points are weighted by their 1σ uncertainty, and the kernel bandwidth is selected according to Scott’s rule (D. W. Scott 1992). The Nakano Note distribution is more similar to the distribution from P. A. Dybczyński & M. Królikowska (2016), with nearly all of the objects having $1/a_0 > 0$ compared to the MPC distribution.

the same color-versus- r_h trend (Figure 12). However, no “new” comet with a heliocentric distance less than ~ 1.5 au was observed.

4.3. Morphology

We assessed the coma morphology of the six comets that exhibited a $g-r$ color decrease within 3 au of the Sun (Figures 13, 14, and 15). The results are summarized in Table 4. Two comets displayed clear jets in the enhanced images: C/2021 A1 (Leonard) and C/2022 E3 (ZTF). They were the only comets observed within 1 au of Earth and the only comets of the six with $1/a_0$ values outside of the Oort spike, suggesting that they are not dynamically new.

The enhanced gas images of the four returning comets show little to no asymmetry in the coma, but they were also observed further from the Sun than the DNCs (Table 4). Very faint asymmetries may be present in C/2021 E3 (ZTF) and C/2021 T4 (Lemmon). C/2021 Y1 (ATLAS) and C/2022 A2 (PANSTARRS) were the most distant observations of the six with a geocentric distance $\Delta \sim 2.3$ au and $\Delta \sim 1.6$ au, respectively. No structure in the coma was detected in the enhanced gas images, which could be due to isotropic outgassing, or the comets were too distant and too faint to detect asymmetries (which can be $\lesssim 10\%$ of the brightness at a given cometocentric distance; M. M. Knight et al. 2023). We

discuss this idea further in Section 5.3. All four of these comets have $1/a_0$ values that indicate that they are dynamically new.

When creating a gas image (described in detail in Section 3.3), we scaled a “dust” r image before subtracting it from the g image, essentially removing the dust features from the image. Therefore, the scale factor can be converted to a dust color for each image. For our sample of six comets, we found that five of them had dust colors $g-r \sim 0.50-0.55$, which is within 2σ of the mean $g-r$ colors of the entire LOOK sample. The exception is C/2022 E3 (ZTF), which had a “dust color” of $g-r = 0.75$ mag. This redder color does not necessarily represent the true color of the dust, as it could be caused by gas contamination in the r bandpass, such as NH_2 (C. Adami et al. 2023), or relatively larger dust grains (L. Kolokolova et al. 2001).

4.4. Disintegrations

C/2021 A1 is one of the two comets in our sample that disintegrated. It was notably bright, reaching a peak apparent magnitude brighter than 3, which led to extensive study (e.g., S. Faggi et al. 2023; D. Jewitt et al. 2023). Prior to its disintegration, a decrease in the brightening rate was observed starting in mid-November, a finding that was corroborated by other observers.²¹ Multiple outbursts were reported after our observations ended throughout the month of December (e.g., J. Crovisier et al. 2021). D. Jewitt et al. (2023) argued rotational instability as the most plausible disruption mechanism, accelerated by the sublimation of buried volatiles.

Though C/2021 A1 is considered to be disintegrated by many (e.g., D. Jewitt et al. 2023), several postperihelion observations have been reported to the Comet OBServation database.²² Therefore, C/2021 A1 may not have fully disintegrated. This may be similar to the case of comet C/2019 Y4, which seemed to disrupt at first but ended up surviving (Q. Ye et al. 2021). Since we were unable to recover the comet in our own observations, we consider this comet disrupted for the purposes of this paper (see Section 5.2).

As C/2021 O3 approached solar conjunction, it became unobservable after reaching solar elongation angles of less than 60° . It was expected to reach a perihelion of $q = 0.29$ au on 2022 April 20. However, it was found to have disintegrated on 2022 April 29 (Q. Zhang et al. 2022), making it the second disintegrated comet in our sample. C/2021 O3 had the most negative reciprocal semimajor axis of the sample with $1/a_0 = -4.2 \times 10^{-5} \text{ au}^{-1}$ —a value similar to $1/a_0 = -4.3 \times 10^{-5} \text{ au}^{-1}$, the reciprocal semimajor axis of C/2007 W1 (Boattinni), which has been suggested to be a candidate for interstellar origin (P. A. Dybczyński & M. Królikowska 2015).

After C/2021 O3 disintegrated, we observed a diffuse coma in the median-combined g -band image on 2022 May 27 (Figure 16). The comet cannot be clearly seen in the r images, suggesting a high gas-to-dust ratio. We determined an upper limit of $g-r < -0.78$ mag, which is much bluer than the $g-r = 0.44 \pm 0.07$ mag observed before disruption.

After the cutoff date for this study, C/2021 Y1’s activity index continued to decrease through perihelion, and the comet was not observed using the LCO network postperihelion. We recovered the comet on 2024 March 6 using the European Southern Observatory’s 8.2 m Very Large Telescope and found

²¹ <https://groups.io/g/comets-ml/message/30254>

²² <https://www.cobs.si/>

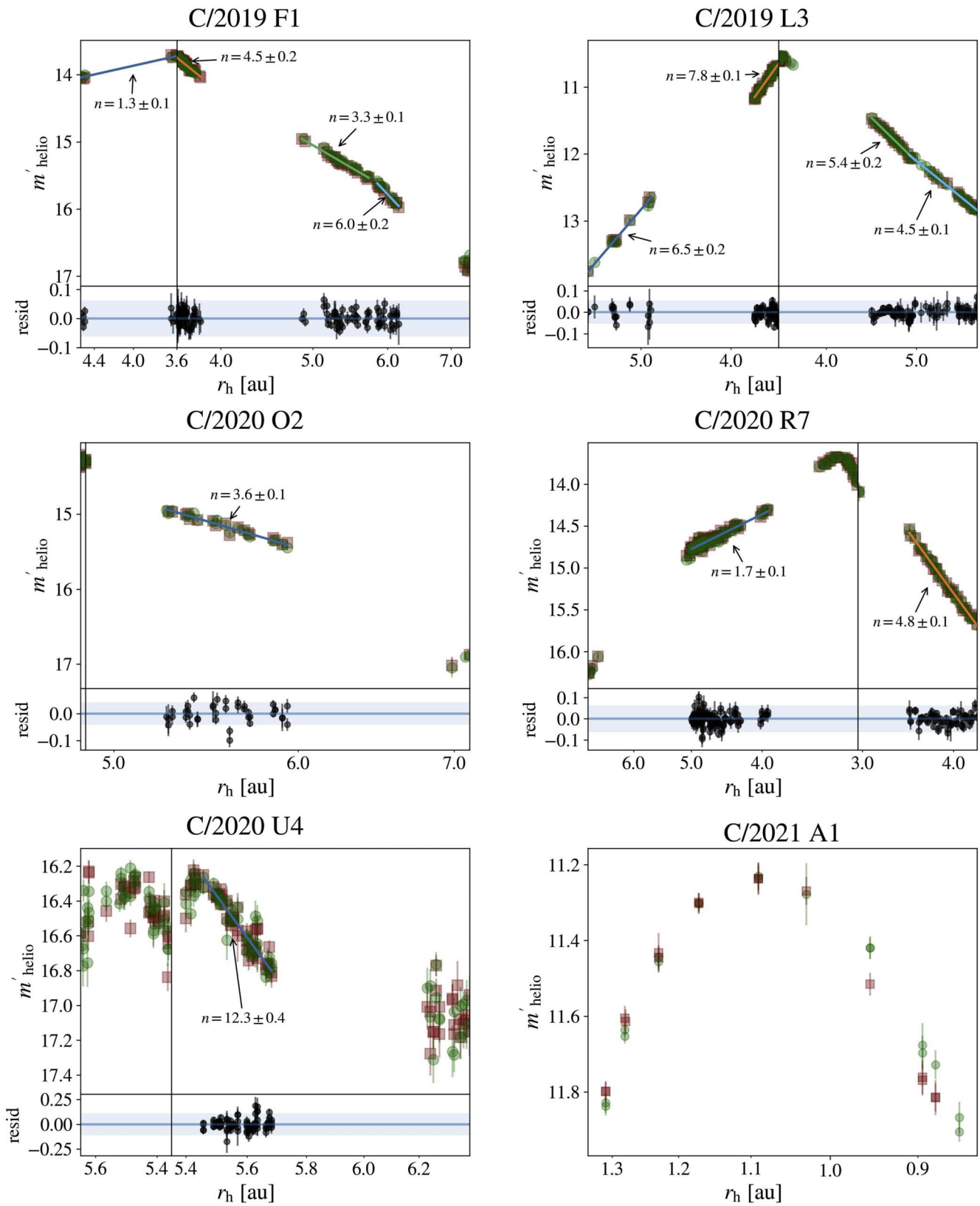


Figure 3. Lightcurves for six objects. For each comet, the upper panel(s) show the variation of m'_{helio} with heliocentric distance using a $5''$ aperture. The red squares represent the r magnitudes, and the green circles represent the g magnitudes shifted by the $g - r$ color, which is listed in Table 3. The solid lines represent the best-fit activity index n to the r and scaled g magnitudes for each section, determined by the least-squares method. The bottom panel(s) show the residuals of the fit, and the shaded region is the median 2σ magnitude error. Perihelion is the vertical line separating preperihelion (left panels) and postperihelion (right panels), and the x -axis is in log scale.

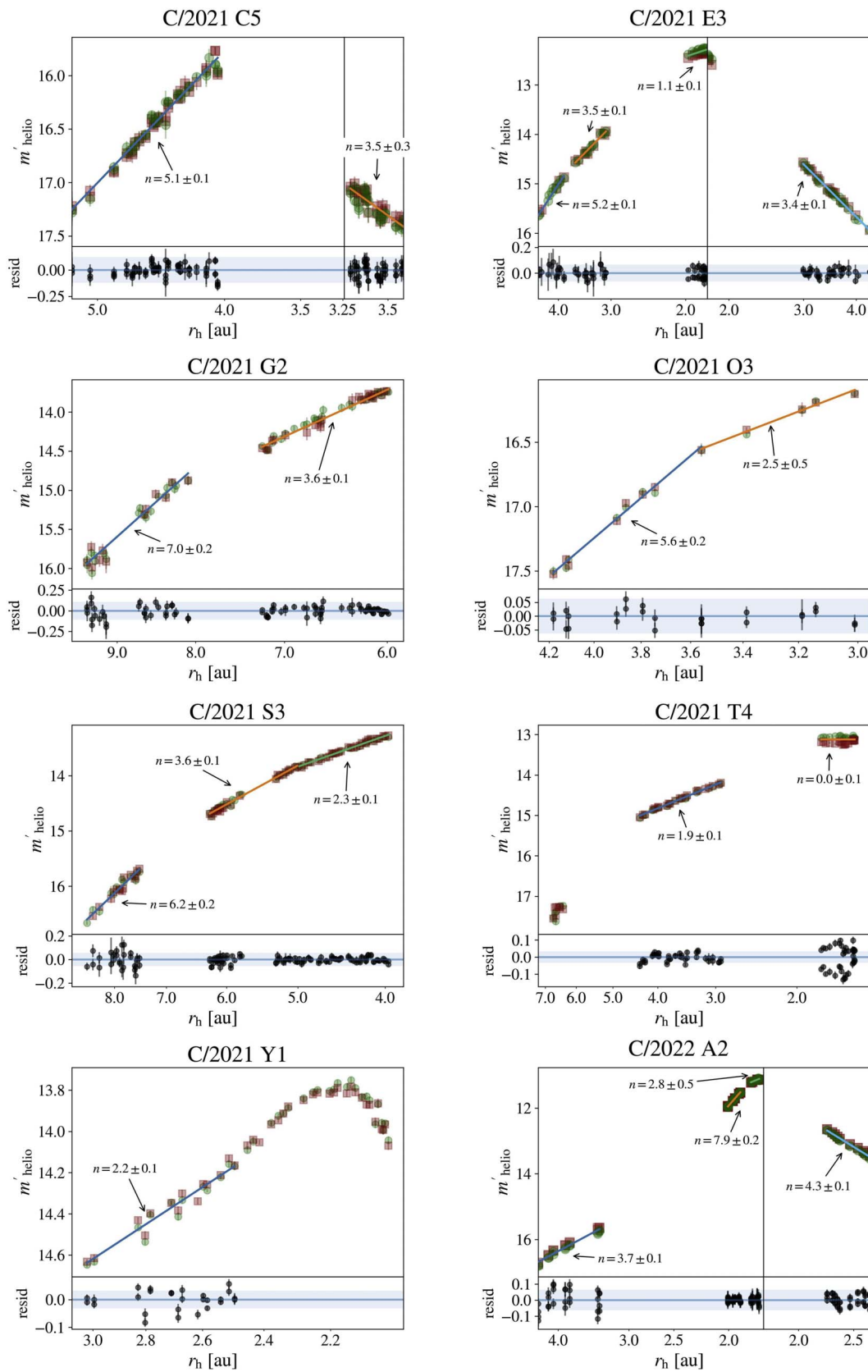


Figure 4. Lightcurves for eight objects as described in Figure 3.

it to be much fainter than expected, with an r magnitude of 21.01 ± 0.07 . JPL Horizons predicted a V magnitude of 17.6. Furthermore, the comet was found to be offset from the

predicted JPL ephemeris by $4''56$, implying strong nongravitational forces and suggesting that C/2021 Y1 may have at least partially disintegrated.

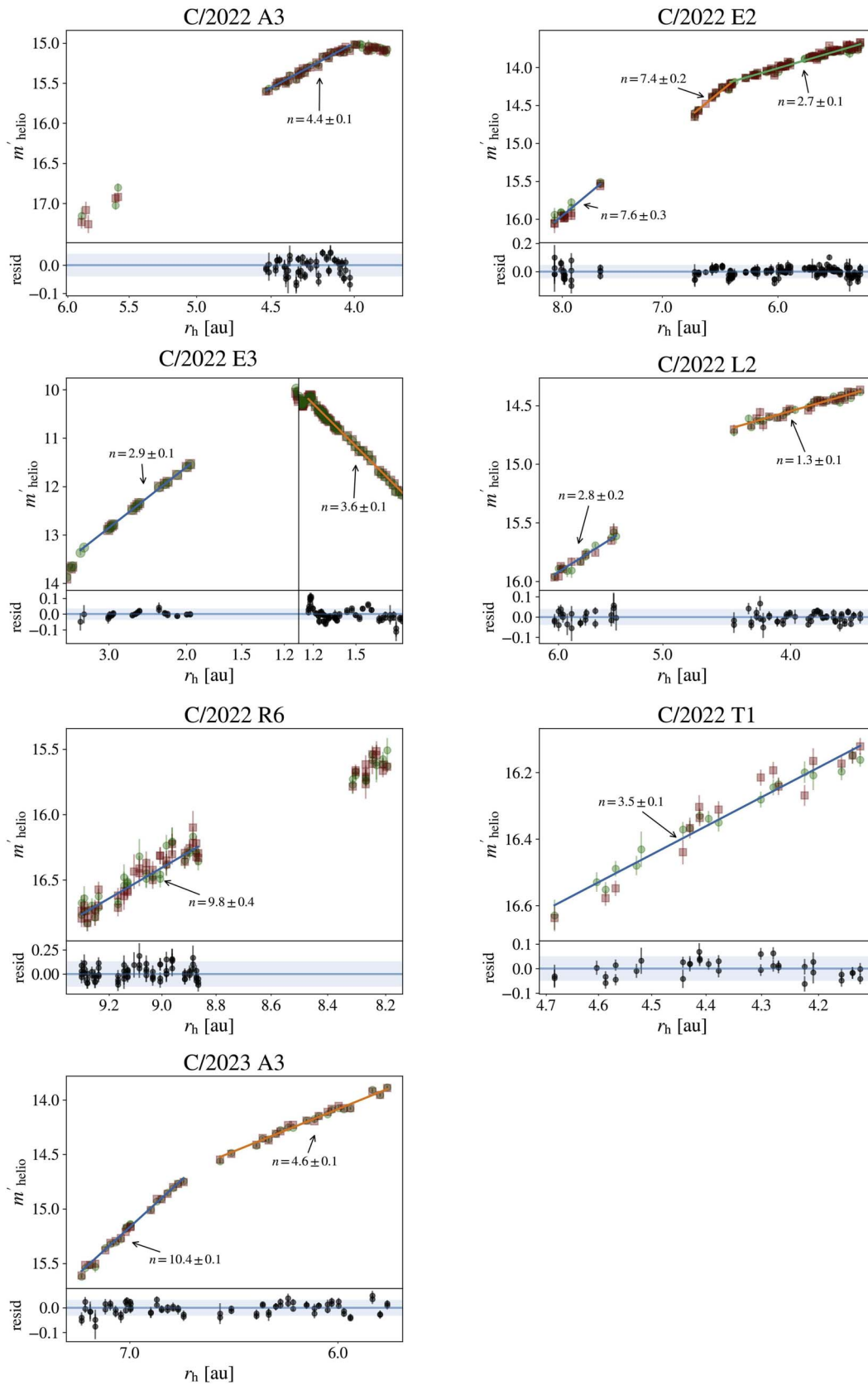


Figure 5. Lightcurves for seven objects as described in Figure 3.

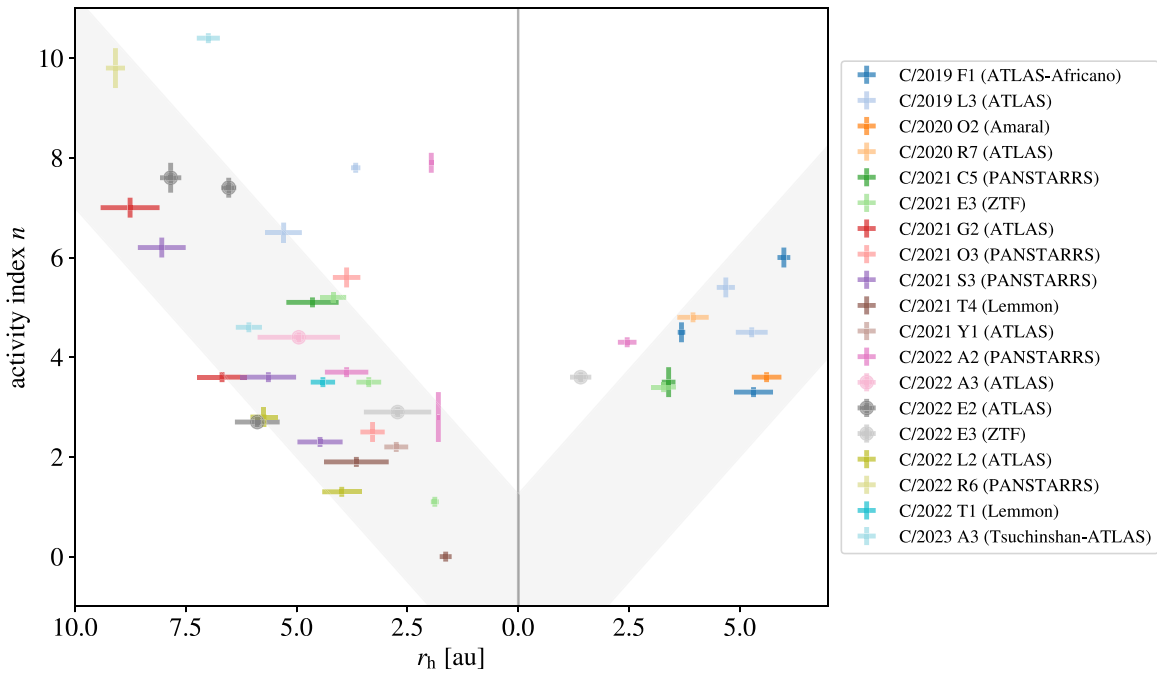


Figure 6. The activity indices for the sample vs. heliocentric distance, where each color is an individual comet with multiple n values. The error bars show the range of heliocentric distance (horizontal) and the 1σ error on the activity index (vertical). Circular markers are returning comets, while the plus signs are DNCs. The activity index is observed to decrease (flatten) with decreasing heliocentric distance for individual comets and the entire sample. The trend is highlighted using a gray shaded region between $n = r_h + 1.25$ and $n = r_h - 3$. Two objects that do not fall into this trend are C/2019 L3 and C/2022 A2, which experienced a “surge” in brightness near perihelion. These comets (as well as C/2023 A3) are outside of the gray shaded region preperihelion.

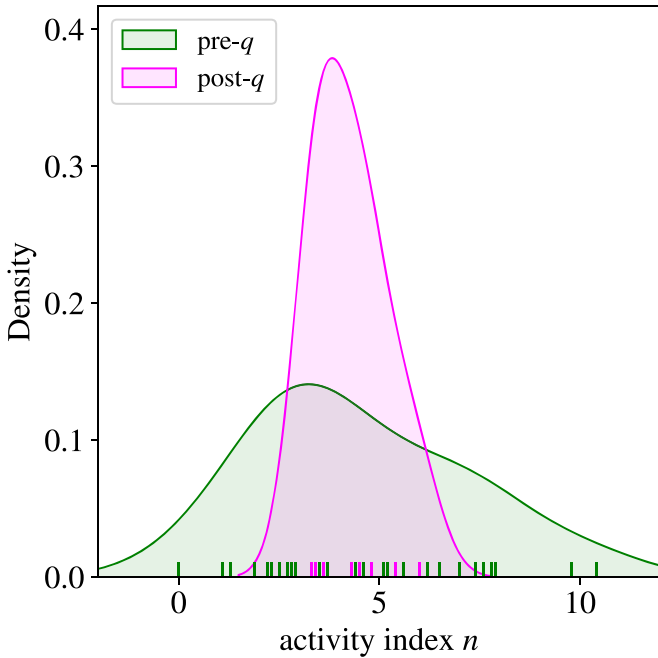


Figure 7. A kernel density plot showing the distribution of the preperihelion activity indices (green) vs. postperihelion (magenta) for our entire sample. We include all activity indices described in Table 2, so a single object will potentially have multiple activity indices. Preperihelion, comets display a wide range of activity indices, while postperihelion is limited to $n \sim 3-6$.

5. Discussion

5.1. Heliocentric Distance Effects on Brightening Rates

DNCs have been observed to (1) be more active (e.g., K. Sárneczky et al. 2016; I. Kulyk et al. 2018) and (2) have a shallower increase in brightness compared to returning comets

(e.g., F. L. Whipple 1978; M. F. A’Hearn et al. 1995). These trends inspired the idea that DNCs may rapidly brighten at large heliocentric distances and brighten more slowly near perihelion (e.g., J. H. Oort & M. Schmidt 1951; F. L. Whipple 1978). However, previous studies of the brightening rate were based on observations when $r_h \lesssim 3$ and therefore did not include the rapid brightening phase of the lightcurve. Our study provides evidence for the hypothesized distant brightening phase. Suggested drivers of the distant rapid brightening include the sublimation of a “frosting” of highly volatile material from irradiation by galactic cosmic rays while in the Oort cloud (F. L. Whipple 1978; R. E. Johnson et al. 1987) and/or the sublimation of ices more volatile than water (i.e., CO, CO₂; K. J. Meech & J. Svoren 2004). That said, D. Marshall et al. (2019) found that a single slope does not sufficiently fit water production trends over a wide heliocentric distance. We do not find evidence that this distant brightening varies between new and returning comets, which we discuss further in Section 5.3.

Certain comets in our study displayed a gradual decline in the activity index (e.g., C/2021 S3, C/2021 G2), while other comets exhibited distinct breaks in the lightcurve (e.g., C/2022 E2). The breaks in the lightcurve could indicate sudden changes in an activity driver (e.g., initiation, plateauing, or exhaustion). The heliocentric distance where the break occurs is different for each comet, so a specific mechanism is unable to be determined. The gradual decline in activity index is explored further in Section 5.4.

Previous studies have reported that DNCs have a shallower brightening rate preperihelion than postperihelion, while returning comets have a steeper rate both pre- and postperihelion (e.g., F. L. Whipple 1978; M. F. A’Hearn et al. 1995). Our data show that only comets with $q < 3$ au (where H₂O sublimation dominates and most of the observations from

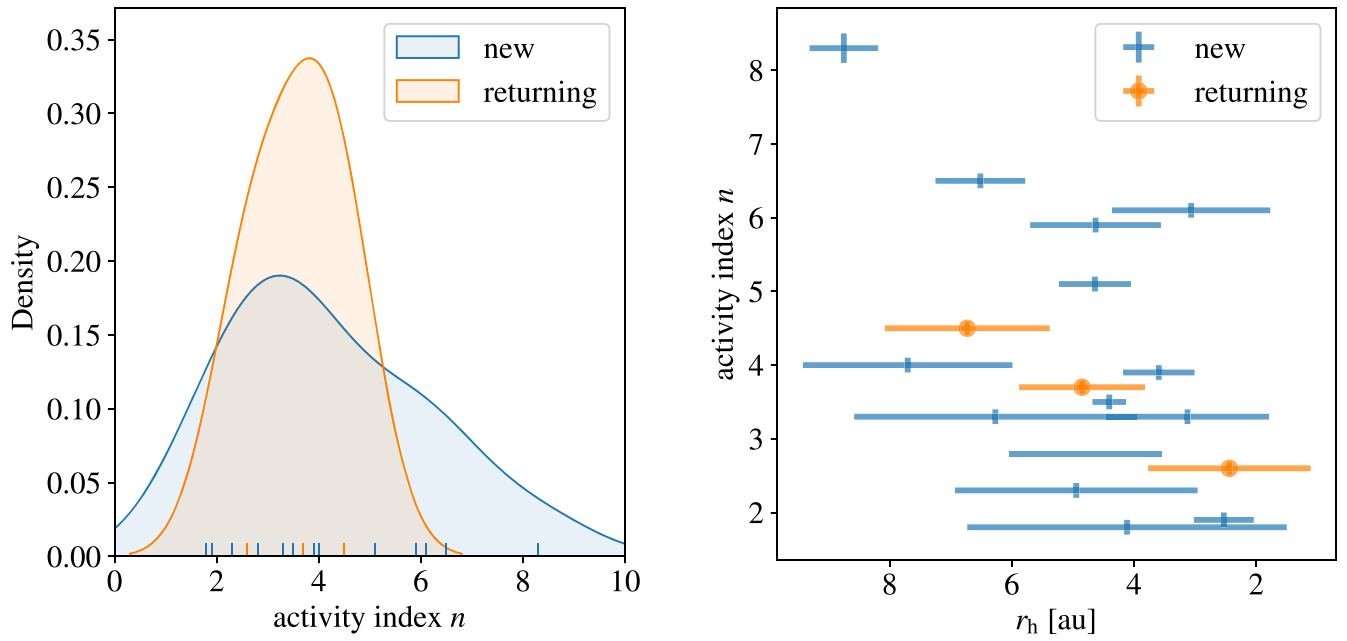


Figure 8. Left: a kernel density plot showing the distribution of the activity indices fit across all perihelion observations for “new” (blue) vs. returning (orange) comets using a threshold of $1/a_0 = 4.0 \times 10^{-5} \text{ au}^{-1}$. The value for each comet is shown as a small vertical line at the bottom of the figure. The two populations are consistent within the uncertainties. Returning comets exhibit a narrow distribution of activity indices with an average of $n = 3.7 \pm 0.7$, whereas “new” comets have a broad distribution of $n = 4.2 \pm 1.9$. Right: the overall perihelion activity index for each object in our sample. The error values show the range of heliocentric distance and the 1σ error on the activity index. The blue plus signs represent “new” comets, while orange circles represent returning comets.

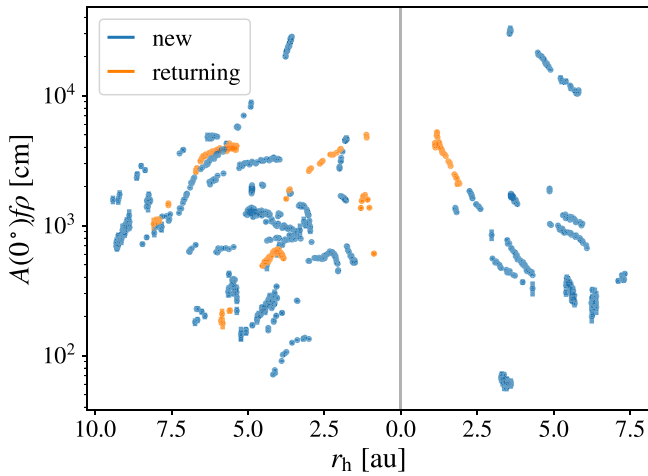


Figure 9. $A(0^\circ)fp$ (an aperture-independent quantity used as an estimator for dust production) vs. heliocentric distance for all comets in our sample, where orange points represent returning comets and blue points are DNCs using a threshold of $1/a_0 = 4.0 \times 10^{-5} \text{ au}^{-1}$. We find no clear trend with $1/a_0$ or r_h .

previous studies occurred) exhibit an activity index $n \sim 2\text{--}3$ that increases to $n \sim 4$ postperihelion (e.g., C/2021 E3, C/2022 E3). In contrast, all LPCs with $q > 3$ au maintained higher activity indices both pre- and postperihelion (e.g., C/2019 F1, C/2019 L3). This suggests that water-ice sublimation or the increase in activity within 3 au of the Sun is related to the asymmetrical brightening/fading rates. This result could be caused by a faster depletion in accessible water ice compared to accessible hypervolatiles. Perhaps the increased activity creates a thicker dust mantle (i.e., an ice-free layer at the surface of the nucleus), so that water ice is less accessible, but the hypervolatiles can still be accessed at greater depths at lower temperatures. A possibly related effect has been observed in the JFC population at 3–7 au, where comets with

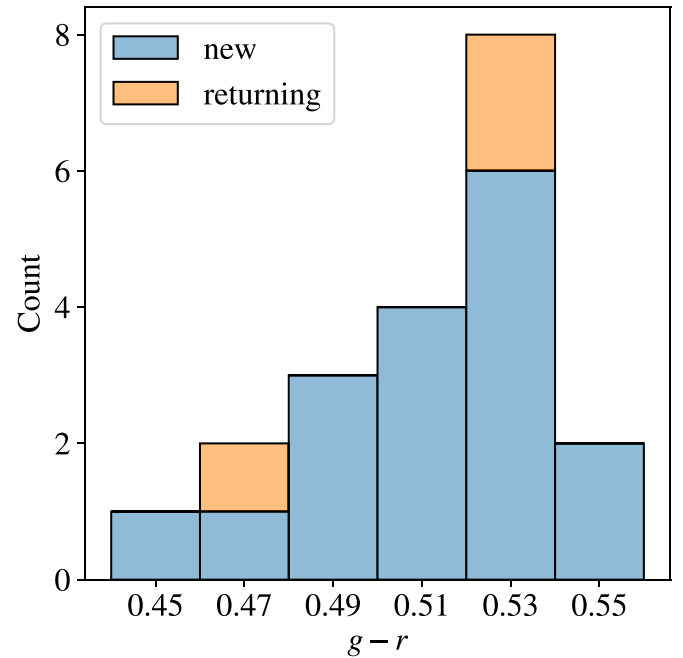


Figure 10. A stacked histogram of the color distribution of “new” (blue) vs. returning (orange) comets using a threshold of $1/a_0 = 4.0 \times 10^{-5} \text{ au}^{-1}$ when $r_h > 3$ au. There is no difference in color where “new” comets exhibit an average color $g - r = 0.51 \pm 0.03$ mag and returning comets have $g - r = 0.51 \pm 0.02$ mag. We note that the conclusion is broad because we only have three returning comets and that the uncertainty for each data point is larger than the histogram bin width. Comet C/2021 A1 is not included because the observations only occurred when $r_h < 3$ au.

smaller perihelion distances tend to have less activity in this heliocentric distance regime than those with larger perihelion distances (M. S. Kelley et al. 2013), possibly due to a thicker insulating surface layer for JFCs with small perihelion

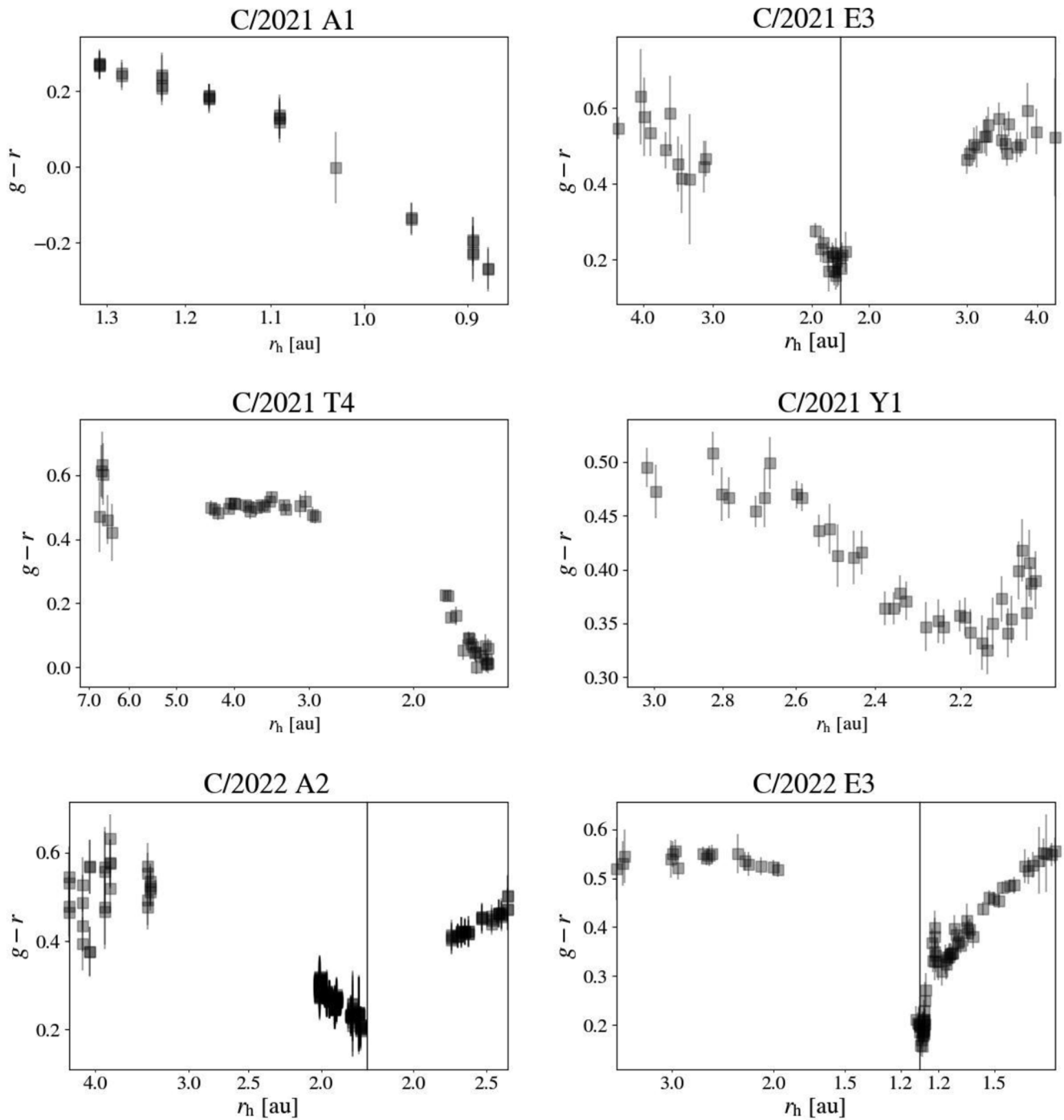


Figure 11. The evolution of $g - r$ with heliocentric distance using a 20,000 km aperture. Each point is one visit, and the error bars represent the 1σ error. The x -axis is in log scale.

distances. Our results still agree with prior studies, because those observations occurred when objects were less than 3 au from the Sun.

5.2. Drivers of Sudden Brightness Change

Seven comets in our sample experienced a preperihelion peak in intrinsic brightness ($n < 2$) out of 10 comets where such a peak could be reliably determined. Three of those seven had a more rapid decrease (C/2021 A1, C/2020 R7, and C/2021 Y1), while the other objects (C/2021 E3, C/2021 T4,

C/2022 A3, and C/2022 L2) have a more shallow decrease or fading rate comparable to the prior brightening rate. Such changes in brightness could be caused by seasonal effects where the illuminated surface area of a nonspherical nucleus varies due to the position of the rotational pole (e.g., P. R. Weissman 1988; D. Schleicher 2007). Similarly, changes in the orientation of asymmetries in the coma (e.g., jets) or the tail could also lead to a change in apparent total brightness, referred to as projection effects. Other possibilities include a decrease in activity due to the depletion of volatiles in the upper surface layers. For C/2020 R7, the rapid decrease was

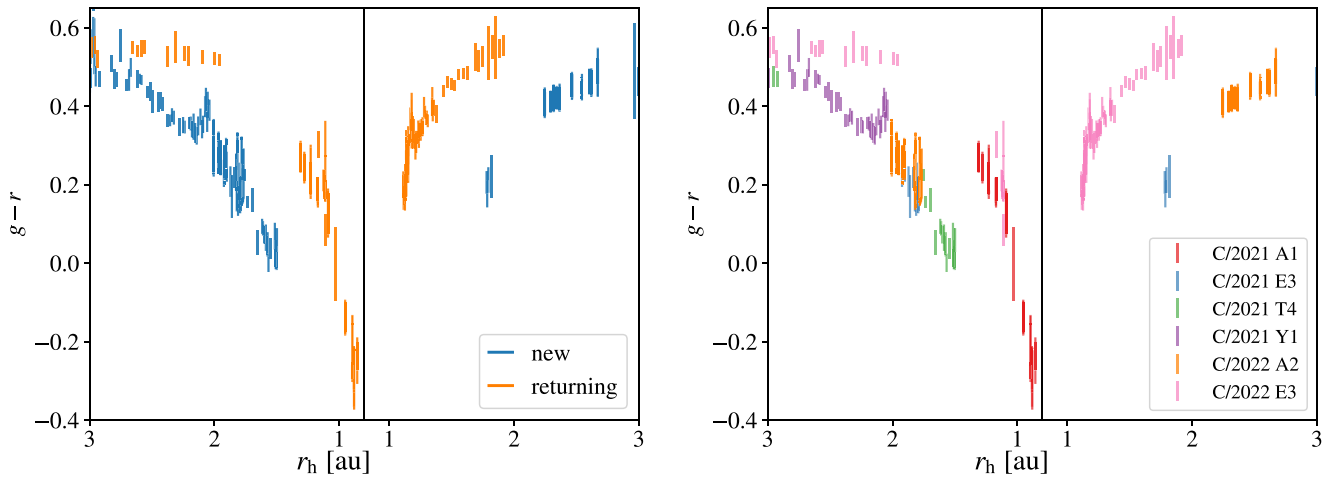


Figure 12. The evolution of $g - r$ color with heliocentric distance within 3 au of the Sun. Left: blue represents the data for new comets and orange for returning. Right: each color represents a different comet. The comets that change to a bluer color do so within 3.0 au from the Sun. Returning comets become bluer within 2 au from the Sun.

followed by a return to a steady activity index postperihelion, suggesting that seasonal effects were responsible for the change in activity in this comet. However, C/2021 Y1’s activity index continued to decrease through perihelion until the comet at least partially disintegrated.

Two other objects in our sample either partially or fully disintegrated near perihelion: C/2021 A1 and C/2021 O3. They have the smallest perihelion distances of our sample with $q = 0.61$ au for C/2021 A1 and $q = 0.29$ au for C/2021 O3. Before disintegration, both comets decreased in brightness (Figure 3; M. Evangelista-Santana et al. 2023). They also became spectrally bluer as their brightness decreased (Figure 11; M. Evangelista-Santana et al. 2023). Other comets in our sample with $q > 1$ au followed these trends and did not disintegrate (e.g., C/2021 T4), so this is unlikely to be a diagnostic for future disintegration as much as perihelion distance and H magnitude, which is used as a proxy for size (J. E. Bortle 1991; Z. Sekanina 2019). However, our last observations of C/2021 A1 and C/2021 O3 (i.e., the dust cloud) are the bluest points of our sample, which is likely related to an excess of outgassing prior to and during disruption.

In the case of C/2021 A1, the dramatic decrease in brightness appears to be related to the phase angle correction. Although the dust phase function used may not be the optimal fit, it would require an exceptionally unusual phase function to make C/2021 A1 exhibit a brightening slope comparable to that of other objects.

We manually inspected all lightcurves for evidence of outbursts but found none. Cometary outbursts are short-lived changes in the mass-loss rate, observable as discontinuities in cometary lightcurves. The discontinuity is followed by a return to the nominal brightness as the ejected material disperses and exits the photometric aperture. The brightening timescales for such events tend to be a few hours or less (e.g., H. H. Hsieh et al. 2010; J.-B. Vincent et al. 2016b; T. L. Farnham et al. 2019), and the ejecta can linger near the nucleus for days to weeks or even longer (D. W. Hughes 1990). The sensitivity and ability to detect outbursts depends on the quality of the photometry and therefore changes with apparent magnitude, but generally no short-term discontinuities stronger than -0.2 mag are seen, though C/2021 A1 did have several

outbursts before disintegrating after LOOK stopped observations (Section 4.4).

5.3. DNCs versus Returning Comets

Studies have previously reported $n \sim 2$ for DNCs and $n \sim 4$ for returning comets (see, e.g., review by K. J. Meech & J. Svoren 2004), suggesting that the active area of the surface increases at a higher rate for returning comets compared to DNCs. However, we find that both classes have higher activity indices of ~ 4 when fit over the entire lightcurve (Figure 8). This discrepancy was originally presumed to be due to the heliocentric distance range of our observations. Activity indices are larger further from the Sun (Figure 6), and most of our observations are further from the Sun, causing our overall mean to be higher. If we limit our analysis to data within 5 au of the Sun to compare with other studies, we find activity indices of $n = 2.9 \pm 1.2$ for new comets and $n = 3.7 \pm 0.8$ for returning. It is important to note that we have only three returning comets in our comparison (and two with $r_h < 5$), since we do not include the activity index of C/2021 A1 because of its decrease in brightness.

Previous studies describe DNCs as being more active due to a higher abundance of volatiles (e.g., K. Sárneczky et al. 2016; I. Kulyk et al. 2018). However, we find no trend of $Af\rho$ with dynamical age. Distant discoveries are more active, allowing us to observe them at such distances, and they are most often dynamically new. But when comparing new and returning comets discovered at the same distance, we find that they have similar $Af\rho$ values (Figure 9).

If we assume that DNCs have yet to build up a dust mantle before their first solar passage, then we would expect the surface to be uniformly active. Therefore, any active fraction less than 100% would imply a previous solar passage. Active areas would present themselves in the form of jets or seasonal effects (i.e., lightcurve asymmetries around perihelion), resulting in a suggestion by A. N. Bair et al. (2018) that coma asymmetries could potentially be used as a diagnostic to distinguish new from returning comets. However, the shape of the comet nucleus can affect the heterogeneity of the coma by shadowing certain regions and collimating outflows (J.-F. Crifo et al. 2002; X. Shi et al. 2018). Even though DNCs have been shown to have a larger active fraction than returning comets

C/2021 A1 2021-11-29

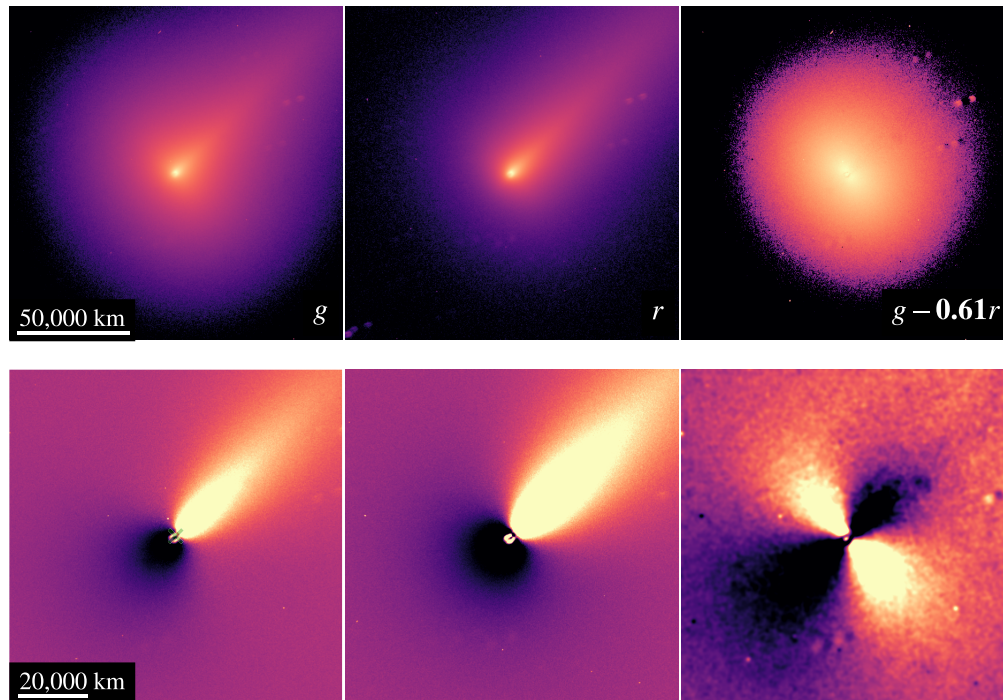


Figure 13. Unenhanced (top row) and enhanced (bottom row) images of C/2021 A1 (Leonard) in the g and r filters (left and middle column) and a “gas” image as described in Section 3.3 (right column) on 2021 November 29, when $r_h = 0.53$ au and $\Delta = 0.58$ au. All images are centered on the optocenter of the comet with north up and east to the left. Light is bright and dark is faint in all panels. The images in the top and bottom row are 200,000 km and 100,000 km across, respectively. The images in the bottom row have been enhanced by subtracting the azimuthal median profile. The morphology of this gas image is very different from the “dust” (r -band) image. Two jets can be seen oriented near positional angles of 40° and 220° (measured from north through east) in the enhanced gas images, seemingly perpendicular to the tail in the northwest direction in the dust images. This image uses the same data and creation process as Figure 11 in T. Lister et al. (2022) but was created independently.

(e.g., M. F. A’Hearn et al. 1995), the presence of asymmetries in the coma morphology and pre- and postperihelion peaks in activity may not be as closely related to the dynamical age as was previously thought. For example, coma asymmetries have been observed in nominal DNCs C/2007 N3 (A. N. Bair et al. 2018) and C/2017 K2 (Y. G. Kwon et al. 2023). Of the six comets we were able to derive a gas image from, the two that were returning (C/2021 A1 and C/2022 E3) have the clearest asymmetries in the coma, while the four new comets show very faint or not visible asymmetries. While this could be related to dynamical age, the range (from most clear, to very faint, to not detected) in asymmetries also correlates with the geocentric distance of the observations (Table 4). Further investigation is needed to determine if there is a difference in the relative strength.

Six comets in our sample reach a heliocentric distance of less than 3.0 au, and all six experience a decrease in $g - r$ color (Figure 12); i.e., they get bluer. Because the g band contains C_2 and C_3 emission lines and the r band is mostly lacking strong gas emission lines, a bluer color suggests an increase in gas flux. The decrease in $g - r$ color occurs at a similar heliocentric distance to the onset of water-ice sublimation. Although the gas species in the g band are not direct daughter products of H_2O , the production rates of C_2 and C_3 are known to be correlated with water production rates (e.g., A. L. Cochran et al. 2012). Therefore, it is likely that the onset of water-ice sublimation at least somewhat contributes to the observed color change. However, the color change may also be influenced by decreasing scale lengths and increasing g factors and gas velocities near the Sun, which would not require an increase in

sublimation. There is a possibility that the increase in water production could be excavating more deeply buried ices causing an increase in volatile sublimation. The four comets that are predicted to be dynamically new all change colors near $r_h \sim 3$ au and at similar rates, whereas the returning comets change colors closer to the Sun. Our results suggest that returning comets may have more deeply buried volatiles or higher dust-to-gas ratios after depleting the upper layers of volatiles on a previous solar passage. In the first case, warming by solar insolation would need to propagate further into the nucleus to cause water-ice sublimation. And a higher dust-to-gas ratio would require smaller heliocentric distances (so that the scale lengths are short enough, etc.) for the C_2 and C_3 production to stand out from the dust in the g band. Both would result in a color change closer to the Sun for returning comets compared to DNCs. Previous research has not established a clear correlation between the dust-to-gas ratio and the dynamical age of comets. For instance, M. F. A’Hearn et al. (1995) found no significant relationship between these variables. U. Fink (2009) reported a correlation between dust-to-gas ratio and perihelion distance, suggesting that the varying dust-to-gas ratio may be due to aging, though the study did not consider the $1/a_0$ values of the sample. Furthermore, there are few studies that cover a wide range of heliocentric distances, and since the dust-to-gas ratio varies with distance from the Sun, limited data may not be sufficient to detect a potential relationship between age and dust-to-gas ratio.

The dynamical history of our objects is important for understanding the potential processes affecting the long-term brightness behavior. However, the reciprocal original

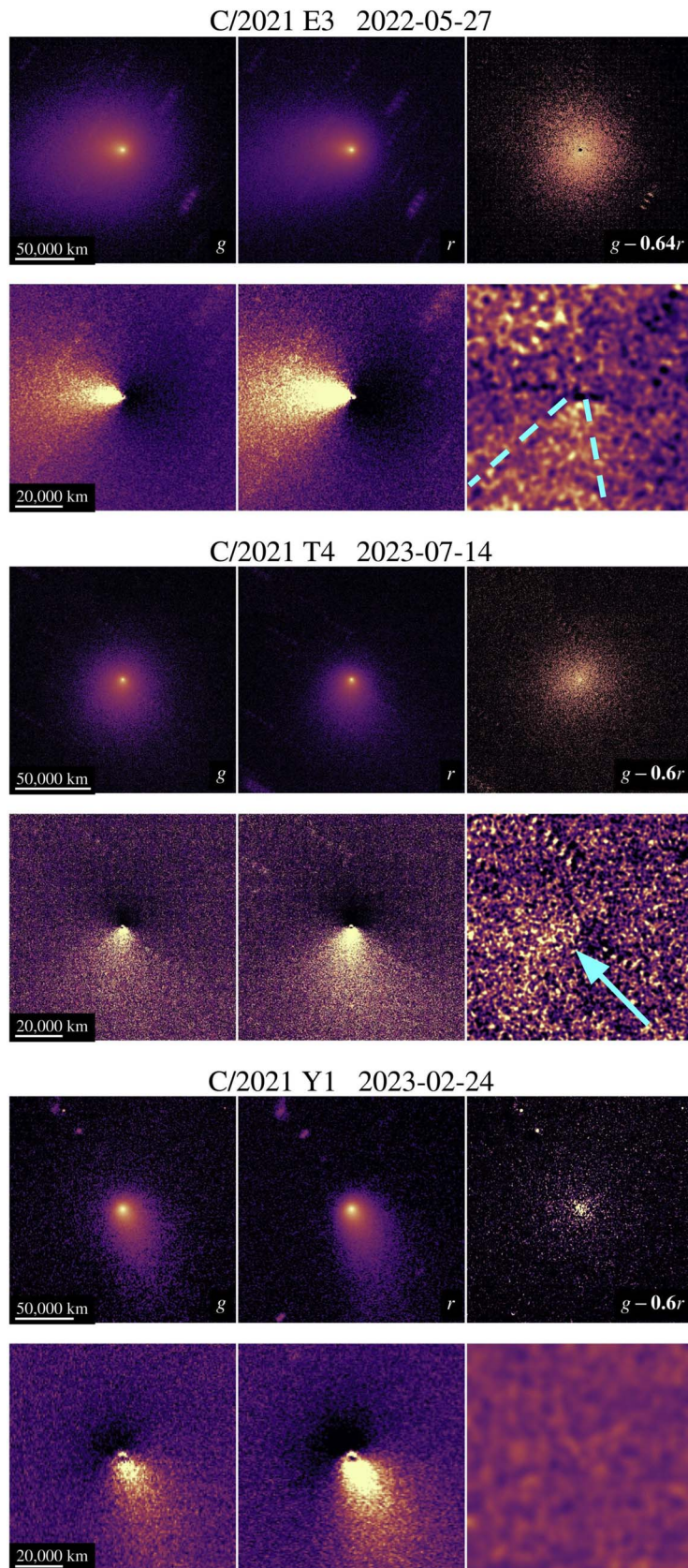


Figure 14. Morphology analysis for three objects as described in Figure 13. We have highlighted the faint features in C/2021 E3 and C/2021 T4 in light blue.

semimajor axis $1/a_0$, which we use as a proxy for dynamical age, is likely the most uncertain variable of our analysis. The models used to determine $1/a_0$ require a long data arc that

many of our comets do not yet have. Additionally, there is no clear threshold of $1/a_0$ that separates new and old comets. Conducting further reverse orbit integrations to determine the

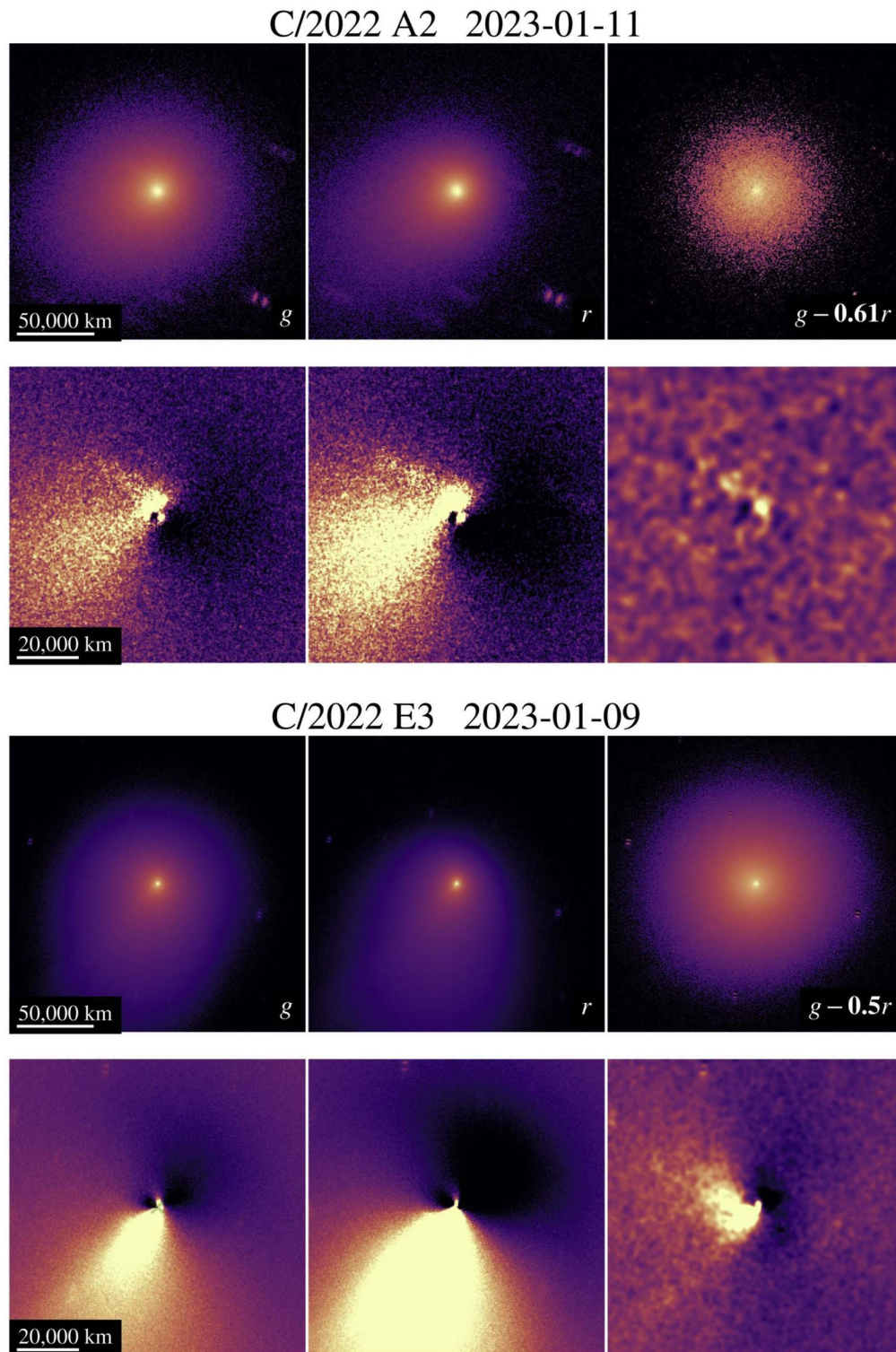


Figure 15. Morphology analysis for two objects as described in Figure 13.

previous perihelion distance q_{prev} would give a more precise look at the prior heating experienced by these objects (P. A. Dybczyński & S. Breiter 2022). Such integrations require the implementation of galactic tides and stellar perturbers, which is not a trivial process (P. A. Dybczyński & M. Królikowska 2022). Currently, only five objects in our sample have a previous perihelion distance reported in the CODE Catalog (C/2019 F1, C/2019 L3, C/2020 O2, C/2020

R7, and C/2020 U4), and all of them have a q_{prev} greater than 400 au.

5.4. Predicting Brightness Behavior

Early accurate predictions of activity for distant comets are especially critical to the selected European Space Agency mission, Comet Interceptor (C. Snodgrass & G. H. Jones 2019;

Table 4
Coma Morphology Figures

Name	Date ^a	r_h ^b (au)	Δ ^c (au)	Scale Factor ^d	Dust $g - r$ ^e	Notes
C/2021 A1 (Leonard)	2021 Nov 29	0.53	0.58	0.61	0.54	Strong jets PA 40° and 220°
C/2021 E3 (ZTF)	2022 May 27	1.79	1.22	0.64	0.48	Maybe faint broad feature PA ~ 190°?
C/2021 T4 (Lemmon)	2023 Jul 14	1.50	0.58	0.60	0.55	Maybe faint feature PA ~ 120°?
C/2021 Y1 (ATLAS)	2023 Feb 24	2.18	2.28	0.60	0.55	No observed asymmetries
C/2022 A2 (PANSTARRS)	2023 Jan 11	1.80	1.62	0.61	0.54	No observed asymmetries
C/2022 E3 (ZTF)	2023 Jan 9	1.11	0.80	0.50	0.75	Wide fans + ion tail PA ~ 130°

Notes.

^a Date the image used for the morphology analysis was taken.

^b Heliocentric distance at the time of the observation.

^c Geocentric distance at the time of the observation.

^d Scaling factor used to create the $g - r$ image.

^e “Dust” color derived from scaling the r image to produce a g image.

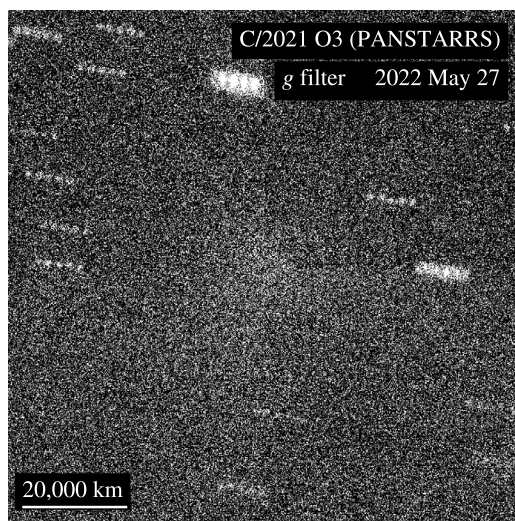


Figure 16. Median-combined g image of the ephemeris location of C/2021 O3 on 2022 May 27, when $r_h = 0.99$ au and $\Delta = 0.79$ au. A diffuse cloud is observed in the center of the image.

G. H. Jones et al. 2024), which will be the first mission to study the nucleus of either an LPC (preferably a DNC) or an interstellar object. To do this, it will employ a novel approach where the mission will be designed and launched before its target is discovered. Comet Interceptor will wait in a parking orbit around the Sun–Earth L2 point, where it can station-keep with very little fuel consumption until a reachable target is found. The spacecraft will depart L2 to encounter the comet following a cruise period of up to 3 yr. A target will most likely need to be selected ~ 3 yr before encounter when the comet will be at a heliocentric distance $r_h \gtrsim 10$ au. Therefore, a reliable prediction of activity near 1 au based on data at large heliocentric distances is required to ensure a successful mission.

The methods for predicting brightness today involve fitting a single activity index across the entire heliocentric distance range. We find a decrease in brightening rate with decreasing perihelion distance consistent with nearly the entire sample. Therefore, an activity index determined further from the Sun should not be extrapolated all the way to perihelion. Furthermore, no single activity index should be used to predict brightness behavior across long timescales and large heliocentric distance ranges. Our study suggests that a more

dynamic prediction model where the activity index decreases through the comet’s inbound orbit would be more accurate. Based on Figure 6, $n = r_h - 1$ would be a more accurate first-order approximation, especially at large r_h . It is important to note that this estimate relates to m'_{helio} , which contains an aperture scaling as described in Section 3.1.

Our analysis shows that within 3 au of the Sun, LPCs consistently become bluer with decreasing heliocentric distance, which aligns with the increase in sublimation and decrease in the dust-to-gas ratio near the Sun. We were surprised to find that published broadband observations through perihelion are relatively rare, likely because most studies use broadband observations at greater heliocentric distances, while observations near the Sun are better suited to spectroscopy or narrowband filters. Consequently, there is more literature on dust-to-gas ratios decreasing as a function of heliocentric distance using narrowband data (e.g., M. F. A’Hearn et al. 1995). Examples of color changes near perihelion include M.-T. Hui & Q.-Z. Ye (2020), who documented a shift toward bluer colors for C/2019 Y4 (ATLAS) before partially disintegrating, and A. V. Ivanova (2020), who observed a similar trend for C/2013 UQ4 (Catalina) as it approached the Sun.

The degree of the change in the brightening rate may be related to dynamical age if we continue the assumption that DNCs have more hypervolatiles and larger active areas. However, a larger sample size across a range of heliocentric distances is needed to thoroughly investigate a prediction model based on dynamical age. Additionally, rapid changes in brightness behavior such as surges and preperihelion peaks are much more difficult to predict—as is the nature of comets.

5.5. Vera Rubin Observatory’s Legacy Survey of Space and Time

With a limiting magnitude of 24.5 (in the r band), the forthcoming Rubin Observatory Legacy Survey of Space and Time (LSST; LSST Science Collaboration et al. 2009; Ž. Ivezić et al. 2019) is projected to detect LPCs at significantly greater heliocentric distances than previously observed, potentially reaching distances beyond 20 au from the Sun regularly. A newly identified comet will be observed many times throughout its orbital path when it is visible from the Southern

Hemisphere, allowing for detailed investigations of its activity as a function of its distance from the Sun. Therefore, the analysis methods used in this study can be used on LSST data, providing a much larger sample to allow for firmer conclusions. However, more than 3 yr of observations are needed before it can be compared to the LOOK data set, which will be at least late 2028 for LSST assuming a start in late 2025.

Over the initial decade, LSST is expected to discover around 10,000 comets (M. Solonoi 2010), thereby providing a substantially larger sample size for LPCs. Such a large amount of data cannot be processed on a case-by-case basis but must be analyzed algorithmically. The LOOK project serves as a test bed for the development of survey and analysis strategies. LOOK was originally intended to study Rubin discoveries, but due to delays, LSST is expected to begin no earlier than late 2025. On the bright side, we are now more prepared for LSST and can make better estimates for future analyses. The data described here can potentially be used in conjunction with a simulated survey to estimate detectability rates and test automated characterization pipelines for LSST.

6. Summary

Since 2020 August, we have used LCO's network of 1 m telescopes and SDSS g and r filters to create a long-term data set with frequent sampling, which we used to characterize the brightness evolution, colors, and coma morphology of distant LPCs. We summarize our results below.

1. The brightening rates flattened with decreasing heliocentric distance for all LPCs. Observations of the rapid brightening portion of the lightcurve will help constrain the potential mechanisms for activity.
2. When predicting future magnitudes, we should consider including a dynamic model where the brightening rate decreases with heliocentric distance compared to the constant value used today.
3. $g - r$ colors are unchanging for all objects beyond ~ 3 au of the Sun and are consistent between DNCs and returning comets with an average color of $g - r = 0.51 \pm 0.03$ mag.
4. When LPCs are within 3 au of the Sun, they consistently exhibit a color change in a 20,000 km aperture, indicating an increase in gas production driven by water-ice sublimation.
5. Returning LPCs experience a surge in gas production closer to the Sun compared to DNCs, suggesting that volatiles are more deeply buried in returning comets or that they have a higher dust-to-gas ratio. The upper layers of the surface may have been depleted on a previous solar passage.
6. We created gas images by subtracting a scaled r image from a g image. The two objects with clear asymmetries were both dynamically old, but they were also observed within 1 au of the Earth. The method can potentially be used to assess gas morphology when narrowband filters (e.g., T. L. Farnham et al. 2000) are not accessible.
7. The addition of more distant comets from the upcoming LSST and the continuation of LOOK will enable better characterization of the population.

Acknowledgments

We sincerely thank the two anonymous reviewers for their valuable feedback, which has greatly strengthened this article. C.E.H. acknowledges support from the Future Investigators in NASA Earth and Space Science and Technology (FINESST) program, grant 80NSSC22K1325, and support from the NASA Solar System Observations (SSO) program, grant 80NSSC22K1714. C.E.H. is supported by an LSST-DA Catalyst Fellowship; this publication was thus made possible through the support of grant 62192 from the John Templeton Foundation to LSST-DA. Parts of this work (the development of NEOexchange) were funded by NASA NEO grants NNX14AM98G and 80NSSC18K0848 to LCO.

M.E.S. was supported by the UK Science Technology Facilities Council (STFC) grants ST/V000691/1 and ST/X001253/1.

R.K. would like to acknowledge the support from "L'Oreal UNESCO For Women in Science" national program for Bulgaria.

This work was also supported by the International Space Science Institute (ISSI) in Bern through ISSI International Team project 504 "The Life Cycle of Comets" (Team Lead: R.K.).

This work makes use of observations from the Las Cumbres Observatory global telescope network. Observations with the LCOGT 1 m were obtained as part of the LCO Outbursting Objects Key (LOOK) Project (KEY2020B-009).

This research has made use of NASA's Astrophysics Data System Bibliographic Services. Data access: raw data products (and basic calibrated data products as described in Section 2.5) supporting this study are available from the LCO Science Archive at <https://archive.lco.global> using the KEY2020B-009 proposal code following a 12 month embargo/proprietary period.









The recovery of comet C/2021 Y1 described in Section 5.2 was based on observations collected at the European Southern Observatory under ESO program 112.25DT.001.

Facility: LCOGT (1 m Sinistro).

Software: astropy (Astropy Collaboration et al. 2018), astroquery (A. Ginsburg et al. 2019), BANZAI (C. McCully et al. 2018), calviacat (M. S. P. Kelley et al. 2019), JPL Horizons (A. Ginsburg et al. 2019), matplotlib (J. D. Hunter 2007), NEOexchange (T. A. Lister et al. 2023), seaborn (M. Waskom 2021), SExtractor (E. Bertin & S. Arnouts 1996).

ORCID iDs

Carrie E. Holt  <https://orcid.org/0000-0002-4043-6445>
 Matthew M. Knight  <https://orcid.org/0000-0003-2781-6897>
 Michael S. P. Kelley  <https://orcid.org/0000-0002-6702-7676>
 Tim Lister  <https://orcid.org/0000-0002-3818-7769>
 Quanzhi Ye (叶泉志)  <https://orcid.org/0000-0002-4838-7676>
 Colin Snodgrass  <https://orcid.org/0000-0001-9328-2905>
 Cyrielle Opitom  <https://orcid.org/0000-0002-9298-7484>
 Rosita Kokotanekova  <https://orcid.org/0000-0003-4617-8878>
 Megan E. Schwamb  <https://orcid.org/0000-0003-4365-1455>

Matthew M. Dobson  <https://orcid.org/0000-0002-1105-7980>
 Michele T. Bannister  <https://orcid.org/0000-0003-3257-4490>
 Marco Micheli  <https://orcid.org/0000-0001-7895-8209>
 Stefanie N. Milam  <https://orcid.org/0000-0001-7694-4129>
 Derek C. Richardson  <https://orcid.org/0000-0002-0054-6850>
 Edward Gomez  <https://orcid.org/0000-0001-5749-1507>
 Joseph P. Chatelain  <https://orcid.org/0000-0002-1278-5998>
 Sarah Greenstreet  <https://orcid.org/0000-0002-4439-1539>

References

- Adami, C., Jehin, E., Aravind, K., et al. 2023, in Proc. Annual Meeting of the French Society of Astronomy and Astrophysics, ed. M. N'Diaye et al. (Strasbourg: SF2A), 511
- A'Hearn, M. F., Belton, M. J. S., Delamere, W. A., et al. 2011, *Sci*, **332**, 1396
- A'Hearn, M. F., Millis, R. C., Schleicher, D. G., Osip, D. J., & Birch, P. V. 1995, *Icar*, **118**, 223
- A'Hearn, M. F., Schleicher, D. G., Millis, R. L., Feldman, P. D., & Thompson, D. T. 1984, *AJ*, **89**, 579
- Astropy Collaboration, Price-Whelan, A. M., Sipőcz, B. M., et al. 2018, *AJ*, **156**, 123
- Bair, A. N., Schleicher, D. G., & Knight, M. M. 2018, *AJ*, **156**, 159
- Bertin, E., & Arnouts, S. 1996, *A&AS*, **117**, 393
- Bortle, J. E. 1991, *ICQ*, **13**, 89
- Brown, T. M., Baliber, N., Bianco, F. B., et al. 2013, *PASP*, **125**, 1031
- Cochran, A. L., Barker, E. S., & Gray, C. L. 2012, *Icar*, **218**, 144
- Crifo, J.-F., Rodionov, A. V., Szegő, K., & Fulle, M. 2002, *EM&P*, **90**, 227
- Crovisier, J., Colom, P., Biver, N., Bockelée-Morvan, D., & Boissier, J. 2021, *CBET*, 5087, 1
- Dybczyński, P. A., & Breiter, S. 2022, *A&A*, **657**, A65
- Dybczyński, P. A., & Królikowska, M. 2015, *MNRAS*, **448**, 588
- Dybczyński, P. A., & Królikowska, M. 2016, *P&SS*, **123**, 77
- Dybczyński, P. A., & Królikowska, M. 2022, *A&A*, **660**, A100
- Evangelista-Santana, M., De Prá, M., Carvano, J. M., et al. 2023, *MNRAS*, **524**, 2733
- Everhart, E. 1967, *AJ*, **72**, 716
- Faggi, S., Lippi, M., Mumma, M. J., & Villanueva, G. L. 2023, *PSJ*, **4**, 8
- Farnham, T. L., Kelley, M. S. P., Knight, M. M., & Feaga, L. M. 2019, *ApJL*, **886**, L24
- Farnham, T. L., Schleicher, D. G., & A'Hearn, M. F. 2000, *Icar*, **147**, 180
- Feaga, L., A'Hearn, M., Sunshine, J., Groussin, O., & Farnham, T. 2007, *Icar*, **190**, 345
- Fernández, J. A., Gallardo, T., & Brunini, A. 2002, *Icar*, **159**, 358
- Filacchione, G., Ciarniello, M., Fornasier, S., & Raponi, A. 2022, *Comets III*, in press (arXiv:2210.02741)
- Fink, U. 2009, *Icar*, **201**, 311
- Ginsburg, A., Sipőcz, B. M., Brasseur, C. E., et al. 2019, *AJ*, **157**, 98
- Guilbert-Lepoutre, A., Besse, S., Mousis, O., et al. 2015, *SSRv*, **197**, 271
- Harrington Pinto, O., Womack, M., Fernandez, Y., & Bauer, J. 2022, *PSJ*, **3**, 247
- Hsieh, H. H., Fitzsimmons, A., Joshi, Y., Christian, D., & Pollacco, D. L. 2010, *MNRAS*, **407**, 1784
- Hughes, D. W. 1990, *QJRAS*, **31**, 69
- Hui, M.-T., & Ye, Q.-Z. 2020, *AJ*, **160**, 91
- Hunter, J. D. 2007, *CSE*, **9**, 90
- Ivanova, A. V. 2020, *AstBu*, **75**, 31
- Ivezic, Ž., Kahn, S. M., Tyson, J. A., et al. 2019, *ApJ*, **873**, 111
- Jewitt, D. 2015, *AJ*, **150**, 201
- Jewitt, D., Kim, Y., Mattiazzo, M., et al. 2023, *AJ*, **165**, 122
- Jewitt, D., Kim, Y., Mutchler, M., et al. 2021, *AJ*, **161**, 188
- Johnson, R. E., Cooper, J. F., Lanzerotti, L. J., & Strazzulla, G. 1987, *A&A*, **187**, 889
- Jones, G. H., Snodgrass, C., Tubiana, C., et al. 2024, *SSRv*, **220**, 9
- Kelley, M. S., Lindler, D. J., Bodewits, D., et al. 2013, *Icar*, **222**, 634
- Kelley, M. S. P., Bodewits, D., Ye, Q., et al. 2019, in ASP Conf. Ser. 523, *Astronomical Data Analysis Software and Systems XXVII*, ed. P. J. Teuben et al. (San Francisco, CA: ASP), 471
- Kelley, M. S. P., Kokotanekova, R., Holt, C. E., et al. 2022, *ApJL*, **933**, L44
- Kelley, M. S. P., & Lister, T., 2022 Calviacat: Calibrate Star photometry by Catalog Comparison, Astrophysics Source Code Library, ascl:2207.015
- Knight, Y. G., Holt, C. E., Villa, K. M., Skiff, B. A., & Schleicher, D. G. 2023, *ATel*, **15879**, 1
- Kokotanekova, R., Lister, T., Bannister, M., et al. 2021, *ATel*, **14733**, 1
- Kolokolova, L., Jockers, K., Gustafson, B. Å. S., & Lichtenberg, G. 2001, *JGR*, **106**, 10113
- Królikowska, M. 2001, *A&A*, **376**, 316
- Królikowska, M., & Dybczyński, P. A. 2020, *A&A*, **640**, A97
- Kulyk, I., Rousselot, P., Korsun, P. P., et al. 2018, *A&A*, **611**, A32
- Kwon, Y. G., Opatom, C., & Lippi, M. 2023, *A&A*, **674**, A206
- Lister, T., Kelley, M. S. P., Holt, C. E., et al. 2022, *PSJ*, **3**, 173
- Lister, T. A., Gomez, E., Chatelain, J., et al. 2021, *Icar*, **364**, 114387
- Lister, T. A., Gomez, E., Chatelain, J., et al., 2023 NEOexchange: Target and Observation Manager for the Solar System, Astrophysics Source Code Library, ascl:2311.005
- Lowry, S., Fitzsimmons, A., Lamy, P., & Weissman, P. 2008, in *The Solar System Beyond Neptune*, ed. M. A. Barucci et al. (Tucson, AZ: Univ. Arizona Press), 397
- LSST Science Collaboration, Abell, P. A., Allison, J., et al. 2009, arXiv:0912.0201
- Marcus, J. N. 2007a, *ICQ*, **29**, 39
- Marcus, J. N. 2007b, *ICQ*, **29**, 119
- Marsden, B. G., & Sekanina, Z. 1973, *AJ*, **78**, 1118
- Marshall, D., Rezac, L., Hartogh, P., Zhao, Y., & Attree, N. 2019, *A&A*, **623**, A120
- McCully, C., Volgenau, N. H., Harbeck, D.-R., et al. 2018, *Proc. SPIE*, **10707**, 107070K
- McKay, A. J., Kelley, M. S. P., Cochran, A. L., et al. 2016, *Icar*, **266**, 249
- Meech, K. J., Pittichová, J., Bar-Nun, A., et al. 2009, *Icar*, **201**, 719
- Meech, K. J., & Svoren, J. 2004, in *Comets II*, ed. M. C. Festou, H. U. Keller, & H. A. Weaver (Tucson, AZ: Univ. Arizona Press), 317
- Oort, J. H. 1950, *BAN*, **11**, 91
- Oort, J. H., & Schmidt, M. 1951, *BAN*, **11**, 259
- Rickman, H., Festou, M. C., Tancredi, G., & Kamel, L. 1992, in *Asteroids, Comets, Meteors 1991*, ed. A. W. Harris & E. Bowell (Houston, TX: Lunar and Planetary Society), 509
- Samarasinha, N. H., & Larson, S. M. 2014, *Icar*, **239**, 168
- Sárneczky, K., Szabó, G. M., Csák, B., et al. 2016, *AJ*, **152**, 220
- Schleicher, D. 2007, *Icar*, **190**, 406
- Schleicher, D. G., & Bair, A. N. 2011, *AJ*, **141**, 177
- Schleicher, D. G., & Farnham, T. L. 2004, in *Comets II*, ed. M. C. Festou, H. U. Keller, & H. Ass. Weaver (Tucson, AZ: Univ. Arizona Press), 449
- Schleicher, D. G., Millis, R. L., & Birch, P. V. 1998, *Icar*, **132**, 397
- Scott, D. W. 1992, *Multivariate Density Estimation* (New York: Wiley)
- Sekanina, Z. 2019, arXiv:1901.08704
- Shi, X., Hu, X., Mottola, S., et al. 2018, *NatAs*, **2**, 562
- Snodgrass, C., & Jones, G. H. 2019, *NatCo*, **10**, 5418
- Solontoi, M. 2010, PhD thesis, Univ. Washington
- Tonry, J. L., Denneau, L., Flewelling, H., et al. 2018, *ApJ*, **867**, 105
- Tonry, J. L., Stubbs, C. W., Lykke, K. R., et al. 2012, *ApJ*, **750**, 99
- Vincent, J.-B., A'Hearn, M. F., Lin, Z.-Y., et al. 2016b, *MNRAS*, **462**, S184
- Vincent, J.-B., Oklay, N., Pajola, M., et al. 2016a, *A&A*, **587**, A14
- Waskom, M. 2021, *JOSS*, **6**, 3021
- Weissman, P. R. 1988, in *Exploration of Halley's Comet*, ed. M. Grewing, F. Praderie, & R. Reinhard (Springer: Berlin), 873
- Whipple, F. L. 1978, *M&P*, **18**, 343
- Womack, M., Sarid, G., & Wierzbos, K. 2017, *PASP*, **129**, 031001
- Ye, Q., Jewitt, D., Hui, M.-T., et al. 2021, *AJ*, **162**, 70
- Zhang, Q., Ye, Q., Farnham, T. L., & Holt, C. E. 2022, *ATel*, **15358**, 1